

## Experimental investigation of flow past a rotationally oscillating tapered cylinder

Soumarup Bhattacharyya<sup>Ⓛ</sup>,\* Izhar Hussain Khan,<sup>†</sup> Puja Sunil,<sup>‡</sup>  
Sanjay Kumar,<sup>§</sup> and Kamal Poddar<sup>||</sup>

*Department of Aerospace Engineering, Indian Institute of Technology Kanpur, Kanpur, UP-208016, India*



(Received 6 December 2022; accepted 18 April 2023; published 12 May 2023)

The flow downstream of a linearly tapered cylinder executing rotational oscillations is experimentally studied at Reynolds number (based on mean diameter) of 250. The tapered cylinder is forced to rotationally oscillate at various oscillation amplitudes and normalized forcing frequencies. The hydrogen bubble technique is used for visualizing the spanwise wake structure, and the laser-induced fluorescence technique is used for visualizing the streamwise wake structure. The cylinder used in the current study has a taper ratio of 70:1 with a mean diameter of 8 mm. Oblique shedding with an oblique angle of  $16^\circ$  is seen for a stationary cylinder which gradually reduces and eventually changes to parallel shedding with an increase of forcing frequency up to a certain forcing frequency which is also dependent on the oscillation amplitude. Flow visualization revealed the forcing frequencies and amplitudes for which the flow becomes two-dimensional. Spanwise cellular structures are observed for some specific forcing parameters. For an oscillation amplitude of  $3\pi/4$  and normalized forcing frequency of 2, a three-dimensional mode is formed at the upper half of the cylinder with a spanwise wavelength of 1.6. Frequency content of the wake measured by hot-film anemometry showed that the flow is governed by multiple frequencies when cellular structures in the wake are observed. It is seen from hot-film measurements that the range of forcing frequencies for which the wake undergoes lock-on increases with increasing oscillation amplitude. A direct drag measurement technique showed that the drag for a stationary tapered cylinder is  $\sim 10\%$ – $20\%$  less than that of a stationary straight cylinder. Particle image velocimetry (PIV) data revealed that the circulation of spanwise vortices loses its strength as we move from the larger diameter end to the smaller diameter end. The drag coefficient for forcing cases is estimated using the momentum deficit formula by finding the mean and fluctuating velocities obtained from PIV. When the forcing frequency enters the lock-on initiation zone, the coefficient of drag becomes maximum, and with further increase in forcing frequency the drag coefficient decreases. The maximum value of the drag coefficient increases as the oscillation amplitude is increased from  $\pi/2$  to  $3\pi/4$ .

DOI: [10.1103/PhysRevFluids.8.054103](https://doi.org/10.1103/PhysRevFluids.8.054103)

---

\*soumarup@iitk.ac.in

<sup>†</sup>izhar@iitk.ac.in

<sup>‡</sup>pujas@iitk.ac.in

<sup>§</sup>Corresponding author: skmr@iitk.ac.in

<sup>||</sup>kamal@iitk.ac.in

## I. INTRODUCTION

Tapered cylindrical structures are often observed in engineering applications including offshore energy structures, submarines, industrial chimney stacks, and marine risers. Roshko [1] first classified the transition range of Reynolds number for the case of a stationary circular cylinder to be  $150 \leq Re \leq 300$ , after which several studies have been conducted in this regime. Despite the geometric simplicity of a cylinder, this regime is rich in vortex dynamics phenomena and three-dimensional instabilities which mark the onset of turbulence downstream of the bluff bodies and a topic of theoretical interest. Gaster [2] initiated the study of vortex shedding behind a linearly tapered stationary cylinder and in his first work discovered that (for cylinders having a taper ratio of 18:1 and 36:1) the fluctuating velocities in the wake are a combination of two frequencies. This was unlike straight stationary cylinders where it is found to be singly periodic in time. Taper ratio is defined as the ratio of cylinder length to the difference in the diameters at two ends. In his second work, Gaster [3] observed that (for cylinders having a taper ratio 120:1) the flow is composed of spanwise cells of constant shedding frequency. Spanwise visualization of the passively controlled flow around a tapered cylinder was first reported by Taneda [4]. Hammache and Gharib [5] conducted experiments on a straight circular cylinder to study the occurrence of oblique vortex shedding in the laminar wake in the Reynolds number range of  $40 \leq Re \leq 160$ . The reason for oblique shedding was cited to be the nonsymmetric pressure distribution that induced the spanwise flow, although this conclusion was in contrast with the previous findings which state that the oblique shedding is because of the secondary instabilities of the flow and its onset is dependent on Reynolds number. Through his experiments on laminar vortex shedding downstream of a straight circular cylinder, Williamson [6] concluded that the phenomenon of oblique shedding is due to the end/boundary effects, and hence, parallel shedding could be induced by altering the boundary conditions (by slightly angling inwards the leading edge of the end plates).

Jespersen and Levit [7] performed numerical simulations of the unsteady three-dimensional flow downstream of a tapered cylinder at a low Reynolds number,  $Re_{\text{mean}} \approx 125$ , where the vortex dislocation process in the spanwise plane was explained. Gaster's observation of the cellular nature of the flow was also found by Piccirillo and Van Atta [8] using the cylinders of various taper ratios (13:1, 23:1, and 32:1). It was further seen that the difference in shedding frequencies between adjacent spanwise cells was constant. This frequency difference was similar to the lower (modulation) frequency first observed by Gaster [3]. Later it was shown by Piccirillo and Van Atta [8] that this modulation frequency is caused by the process of vortex splitting. During vortex splitting at the boundary between the two cells, one vortex line would break into two. Many studies have been conducted to date which validate the presence of this cellular behavior in the spanwise plane for shear flow past uniform bluff bodies. Kumar *et al.* [9,10] experimentally showed the comparison of vortex shedding patterns in the near wake of a straight and stationary cylinder. Valles and Andersson [11] studied the vortex shedding in the wake behind linearly tapered circular cylinders at a Reynolds number (based on the velocity of the incoming flow and the largest diameter) ranging from 130 to 180 for the two taper ratios 75:1 and 100:1. Numerical analysis showed that the taper-ratio variation gave rise to discrete shedding cells, each with its characteristic frequency and inclination with respect to the axis of the cylinder. Flow visualizations showed that vortex dislocation and splitting occurred in the numerically simulated flow fields. The computer simulations matched well the extensive laboratory experiments reported by Piccirillo and Van Atta [8] for a range of comparable conditions.

Parnaudeau *et al.* [12] analyzed the spanwise wake structure behind a tapered cylinder with the help of three-dimensional direct numerical simulation. Narasimhamurthy *et al.* [13] observed that the tapering instigated the flow to be quasi-two-dimensional and gave rise to a pressure-driven secondary spanwise flow. The steady wake showed a substantial variation of pressure along the span. This spanwise variation of the steady wake is associated partly with the local diameter affecting the local  $Re$ . One of the primary motivations for this study was the relatively new experimental observations of Visscher *et al.* [14] with three-component stereo particle image velocimetry (PIV)

which analyzed three-dimensional time-dependent flow behind a cylinder with a taper ratio of 75:1. This approach revealed long time series of the individual velocity components and complete planar views of the instantaneous three-dimensional flow field. The details of single dislocation event and their reoccurrence periodically in longer time spans were obtained by time-resolved recordings. Vortex splitting and dislocation were also observed numerically by Bargi *et al.* [15] while studying vortex-induced vibration downstream of a tapered cylinder. Recent studies of three-dimensional wake downstream of a tapered cylinder with a large taper ratio made by De and Sarkar [16] showed the topology of the shedding signature.

Numerous studies in the last few decades were made where the wake of the cylinder was actively controlled by using certain forcing parameters. These include rotation of the cylinder about its axis, oscillation of the cylinder in the transverse and lateral direction, and imparting rotational oscillation to the cylinder about its axis to alter the flow dynamics. Williamson and Roshko [17] revealed the vortex formation in the wake of a cylinder oscillating laterally. Techet *et al.* [18] performed flow visualization experiments for flow behind a transversely oscillating tapered cylinder with a taper ratio of 4:1 at Reynolds numbers from 400 to 1500. It was discovered that within the lock-on region and above a threshold amplitude, a single frequency of response dominates the entire span and cellular formations cease to occur. In contrast to vortex dislocations, the vortex split remains stable and periodic in the wake region depending on the oscillation amplitude, frequency of oscillation, and local Re. Radi *et al.* [19] experimentally found new three-dimensional modes downstream of a rotating straight circular cylinder in addition to the three-dimensional modes found by Rao *et al.* [20,21] numerically. This experimental study also served as a motivation to find out the three-dimensional modes in the wake of a rotationally oscillating tapered cylinder. A recent wake study by Chikkam and Kumar [22] revealed the influence of the rotation rate  $\alpha$  and hydrophobicity on the structure of the wake of a hydrophobic rotating cylinder at  $Re \approx 200$ . There are numerous two-dimensional studies (in the  $x$ - $z$  plane) on the wake of a rotationally oscillating circular cylinder for various forcing frequencies and amplitudes ([23–25]). Kumar *et al.* [25] showed the flow visualization data for various forcing parameters at a Reynolds number of 185 and found that for some forcing parameters the flow turns three-dimensional. Lock-on parameter space (combination of forcing amplitude and forcing frequencies) where the cylinder oscillation frequency matches the shedding frequency in the wake was revealed. Recently, experiments on a rotationally oscillating cylinder with an attached flexible filament were performed by Sunil *et al.* [26]. Similar diagnostics for characterising the velocity and vorticity field using planar PIV are conducted in this investigation.

In the past, there has been much interest in accurate drag estimation. In the present work drag estimation has been done using the wake defect technique [see Eq. (1) below]. This technique has been used for predicting the sectional drag coefficient behind bluff bodies (originally used by Antonia and Rajagopalan [27]) and has also been referenced in various recent studies, e.g., Konstantinidis and Balabani [28] for a cylinder, Zhou *et al.* [29] for an airfoil, Sharma and Deshpande [30] for a flat plate, Feng and Wang [31] for a circular cylinder with synthetic jets, He *et al.* [32] for square cylinders, and Brennan *et al.* [33] for cylinders with hydrophobic sand:

$$C_d = 2 \int_{-\infty}^{\infty} \frac{U}{U_{\infty}} \left(1 - \frac{U}{U_{\infty}}\right) d\eta + 2 \int_{-\infty}^{\infty} \frac{\overline{v'^2} - \overline{u'^2}}{U_{\infty}^2} d\eta . \quad (1)$$

In this equation, the first term is the momentum deficit of the time-averaged flow field, and the second term is the contribution of the streamwise  $u'$  and cross-stream  $v'$  turbulent fluctuations. The coefficient of drag (global) would depend on the sectional drag coefficient according to the equation

$$C_D = \frac{1}{2L} \int_{-L}^{-L} C_d dy , \quad (2)$$

where  $L$  is the half-length of the cylinder.

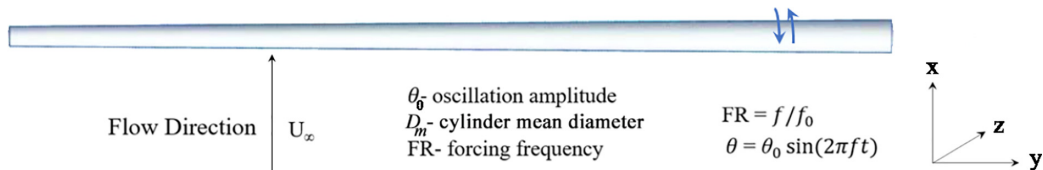


FIG. 1. Schematic of the problem.

Thiria *et al.* [24] undertook the first direct drag measurement experiment on a cylinder performing rotary oscillations in order to investigate the impact of forcing oscillations on the global drag at a Reynolds number of 150. It was seen that the drag coefficient strongly depends on the forcing parameters, which explains why the drag force may be decreased by reducing the strength of the shedding vortices.

Three-dimensional modes in the wake of a rotationally oscillating tapered cylinder have not been studied to the best knowledge of the authors. In this study, the two-dimensional and three-dimensional spanwise flow behind a rotationally oscillating tapered cylinder is studied. The relevant questions that would be answered through this study are (1) How does the taper affect the flow behind the rotationally oscillating cylinder? (2) How do the forcing parameters change the wake behind a tapered cylinder? (3) How do the forcing parameters change the drag behind a rotationally oscillating tapered cylinder? (4) What are the possible reasons for the changes in drag? (5) What are the forcing frequencies and amplitudes where we find distinct three-dimensional modes in a tapered cylinder? Inquiry into these questions will provide good insights into the vortex structures downstream of the tapered cylinder. More importantly, it will provide insight into the evolution of three-dimensional modes in wake of a tapered cylinder in the spanwise plane.  $Re_{\text{mean}}$  (Reynolds number based on mean diameter) was fixed at 250 where the three-dimensionalities are profound for a stationary straight cylinder (both modes, large-scale disturbances mode A and small-scale disturbances mode B, coexist). This will help address some of the questions about the wake downstream of a tapered cylinder and the trends in the evolution of modes under forcing. Furthermore, this study would provide an understanding of forcing parameters that would assist or restrict the formation of three-dimensional modes which eventually would lead to the onset of turbulence. The present experimental study consists of flow visualization using the hydrogen bubble flow visualization technique and laser-induced fluorescence, as well as quantitative study through PIV, direct drag measurement, and hot film anemometry.

The frequencies in the present study are nondimensionalized using  $f_0$ , the vortex-shedding frequency of the stationary straight cylinder whose diameter matched the mean diameter of the tapered cylinder (8 mm). The ratio  $f/f_0$  is called the frequency ratio and is denoted by FR. The schematic of the problem is shown in Fig. 1. The cylinder was forced to oscillate sinusoidally as

$$\theta = \theta_0 \sin(2\pi ft), \quad (3)$$

where  $\theta$  is the angular position of the cylinder,  $\theta_0$  is the oscillation amplitude,  $f$  is the forcing frequency, and  $t$  is time.

## II. EXPERIMENTAL SETUP AND DIAGNOSTICS

The experiments for the present study were performed in a water tunnel with a test section of length 0.46 m, width 0.18 m, and depth 0.25 m in the Fluid Dynamics Laboratory of the Department of Aerospace Engineering, IIT Kanpur. Water is recirculated in the tunnel using a 1.5 hp variable speed centrifugal pump. The tunnel water temperature is maintained at  $25^\circ\text{C} \pm 1^\circ\text{C}$ . Details of the experimental techniques and diagnostics are provided in the next subsection.

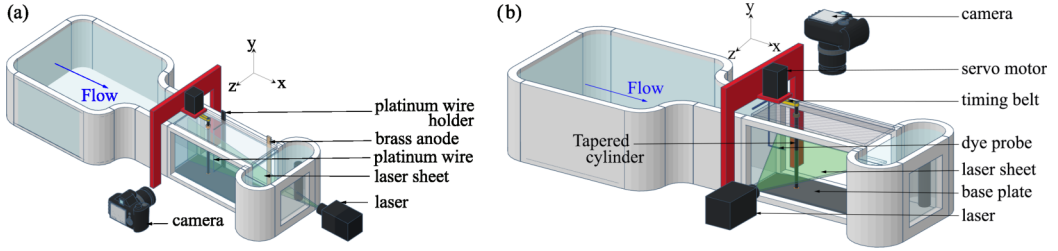


FIG. 2. Flow visualization setup (a) Schematic of the experimental setup for hydrogen bubble flow visualization in the  $x$ - $y$  plane. (b) Schematic of the experimental setup for laser-induced fluorescence visualization in the  $x$ - $z$  plane. A similar setup is used for PIV experiments in the  $x$ - $z$  plane where the dye probe is absent.

### A. Experimental setup

The experiments for the present study are performed in a water tunnel, and the water velocity needed to achieve  $Re_{\text{mean}} = 250$  based on mean diameter  $D_m = 8$  mm is  $u \approx 0.03 \text{ msec}^{-1}$ . The maximum speed of the flow can be  $0.13 \text{ m sec}^{-1}$  and the turbulence intensity is less than 0.5% root mean square (r.m.s.) at the present experimental conditions. A linearly tapered 280 mm long (wetted length) cylinder made of stainless steel was used for the present study. The maximum diameter of the cylinder was 10 mm, and the minimum diameter was 6 mm, which results in mean diameter of 8 mm. The cylinder is oriented spanwise in the tunnel test section such that the wider end is upwards and the narrow end is downwards. The narrow end is fixed with a bearing in the lower black anodized aluminum plate, and the upper end is penetrated through a hole which is carved in the upper perspex plate. This hole is fitted with a bearing in it which allows the rotatory motion of the cylinder. The extended upper end (which is extending above the top perspex plate) is attached to the servo motor with a timing pulley mechanism using a belt to ensure minimum wobbling. The cylinder extends throughout the entire depth of the test section. The level of the water in the test section is such that it touches the base of the top perspex plate. A servo motor is used to provide sinusoidal rotational oscillation to the cylinder. This motor is connected to a servo motor drive which is controlled using a software. The oscillation amplitude is varied using this software. The setup is also connected to a signal generator. The signal generator provided an analog sinusoidal signal of known frequency facilitating the control of cylinder's oscillation frequency.

#### 1. Flow visualization setup

Flow visualization experiments for observing the spanwise ( $x$ - $y$  plane) wake structure were performed using the hydrogen bubble technique. The visualization setup for this method is shown schematically in Fig. 2(a). The hydrogen bubble sheet is produced using a  $50 \mu\text{m}$  diameter platinum wire, acting as the cathode, stretched across the spanwise section of the cylinder. A brass airfoil-shaped plate (to avoid vortex shedding), acting as an anode, was placed at a downstream distance of 400 mm. The vertical platinum wire was moved in the  $y$ - $z$  plane using an XY-traverse to locate the optimum position for three-dimensional spanwise vortex structures to be visible. It was observed while performing the experiments that the best visualization results were achieved when the platinum wire was placed at an optimum distance from the  $x$ - $y$  symmetry plane as also reported by Radi *et al.* [19]. The optimum distance varied with free-stream velocity and forcing conditions, such that it had to be adjusted for each run. Care was taken so that the wire was not placed too close to the cylinder ( $\leq 0.5D$ ) as it can modify the modes and force new modes. A potential difference of 8.5 to 12.5 V was effective for obtaining good quality hydrogen bubbles. A small amount ( $\sim 35$  g) of sodium sulfate was added to the water in the tunnel to promote electrolysis and improve the quality of bubbles. The hydrogen bubbles formed on the platinum wire are swept downstream by the flow to form a bubble sheet. A continuous diode-pumped solid-state 532 nm laser (300 mW) is used from the tunnel end to illuminate the bubbles for hydrogen bubble flow visualization, as

shown schematically in Fig. 2(a). The laser beam was transformed into a sheet using cylindrical lens optics housed in a collimator. The bubbles form bright streaks when they cross the laser sheet. The laser beam collimator was used to adjust the sheet thickness and its alignment. The spanwise flow structures made visible by the illuminated bubble sheet were captured with a Nikon D810 digital video recorder viewing perpendicular to the illumination and flow direction. The camera has a 37 megapixel CCD image sensor and the ability to shoot at 60 fps. The framing rate of the DSLR camera provided an adequate resolution to distinguish the flow structures at a relatively low Re of 250. A Nikon lens with 1:2.8G vibration reduction (VR) and 60 mm macro focal length was mounted onto the camera for acquiring the spanwise wake behind the cylinder. The data were acquired in different phases, but the ones that are presented in this study are of the same phase corresponding to the maximum angular displacement from the center in the clockwise direction when viewed from the top.

A schematic of the experimental setup to obtain data in the streamwise plane ( $x$ - $z$  plane) is shown in Fig. 2(b). Data in the  $x$ - $z$  plane were acquired to link the flow fields in the wake cross section to observations in the  $x$ - $y$  plane from a side perspective. For these measurements, laser-induced fluorescence flow visualization is used. In these cases, a dye probe releasing Rhodamine dye was used and the resulting structures were illuminated by the laser sheet.

## 2. Hot-film measurement setup

The frequency content of the wake is measured by hot-film anemometry using a single-sensor fiber-film probe from Dantec with a heavy quartz coating for use in water. A Dantec miniCTA 54T42 system equipped with two-channel BNC connectors is used for obtaining spectral data. The probe was mounted on a straight holder and inserted from the downstream end of the tunnel with the help of an XY-traverse. This traverse is mounted on a traverse holder (a mounting mechanism). The data were acquired with a sampling rate of 100 K samples/sec/channel by a NI-9125 card at 16 bit resolution for 30 sec. The shedding frequency of the stationary straight cylinder (same diameter as the mean diameter of the tapered cylinder)  $f_0$  was seen to be  $\approx 0.73$  Hz for Re = 250, and this value was used for defining the normalized frequency ratio, FR. The lock-on (where the frequency of the wake matches the cylinder oscillation frequency) dependence on forcing frequency and amplitude was found from the spectrum of streamwise velocity fluctuations at a downstream distance of  $x/D_m = 2$  from the cylinder through hot-film anemometry. The fiber-film probe was kept  $\sim 0.9D$  away from the cylinder center line along the  $z$  axis and in the middle of the vertical extent of the cylinder where the cylinder diameter was  $D_m = 8$  mm.

## 3. Particle image velocimetry setup

PIV data were taken in the water tunnel in the same experimental conditions (but as different realizations) as the flow visualization experiments. The schematic of the PIV setup in the  $x$ - $z$  plane is shown in Fig. 2(b) (only the dye probe used in the flow visualization experiments was absent for the PIV studies). A TSI PIV system using the INSIGHT 4G platform was used to control the CCD camera and firing of the pulsed laser to capture the images. The flow was seeded with 10  $\mu$ m diameter hollow glass spheres and illuminated in a horizontal plane just downstream of the cylinder with a laser sheet. The laser sheet was formed using the cylindrical lens optics in front of the double-pulsed laser (532 nm to 300 mJ/pulse). The laser sheet was focused down to a thickness of less than 0.9 mm. The digital images of the glass spheres (particles) in the plane of the laser sheet were captured using an 8 MP CCD camera for PIV analysis. The size of the captured images was  $2334 \times 1751$  pixels. The physical area covered by the images was 170 mm  $\times$  130 mm, corresponding to a magnification of about 0.052 mm/pixel. The camera acquisition rate for time-averaged PIV was  $\sim 3.6$  Hz. The overall uncertainty in velocity was estimated to be approximately 0.95% of the maximum streamwise velocity, which resulted in a maximum uncertainty of approximately 1.08% and 1.17% in the spanwise vorticity and circulation measured in the study. A multipass FFT window deformation algorithm with a Gauss  $2 \times 3$ -point subpixel estimator was used to perform

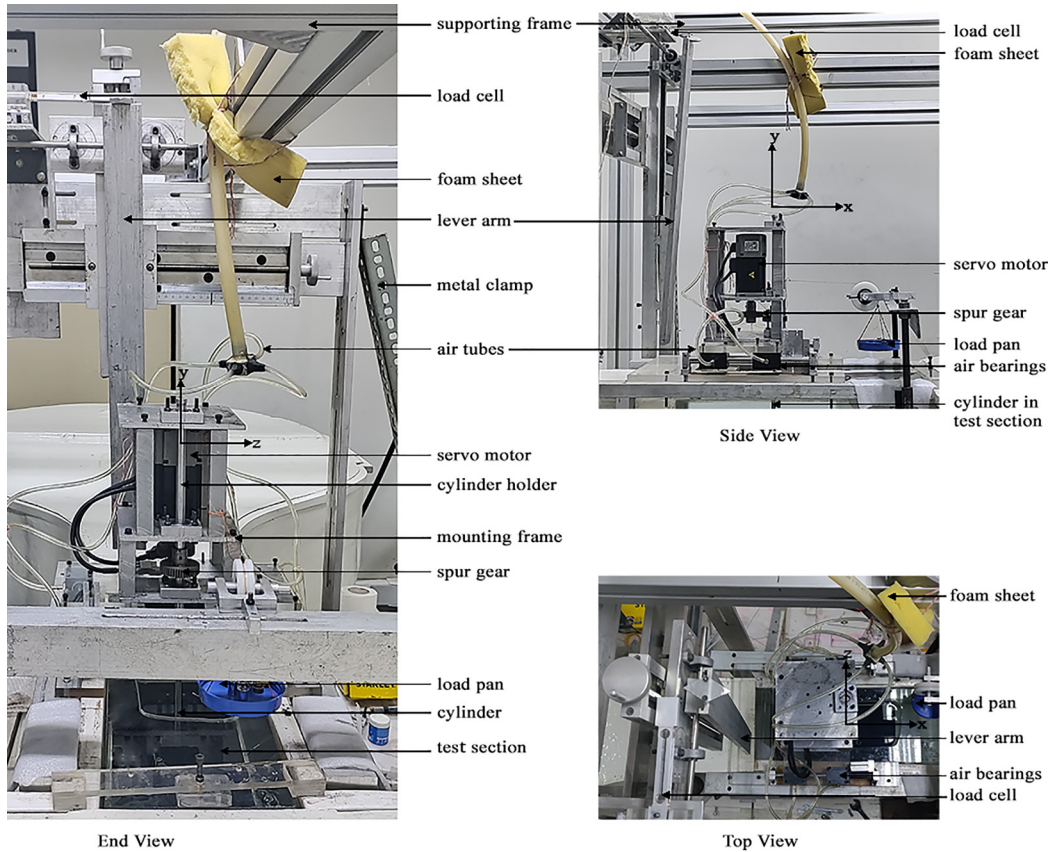


FIG. 3. Experimental setup for direct drag measurement of a tapered cylinder.

the PIV cross-correlation. The laser pulse and camera were synchronized using the synchronizer. The image processing was done using  $32 \times 32$  rectangular interrogation areas with 50% overlap in the vertical and horizontal directions. This resulted in spatial resolution of 1.664 mm ( $32 \text{ pixels} \times 0.052 \text{ mm/pixel}$ ) or  $0.208D$  in the vorticity fields. Frame independence test for phase-locked time-averaged PIV of 100 frames, 200 frames, and 400 frames showed similar results.

#### 4. Direct drag measurement setup

The current setup uses four air bushings (air bearings) to provide a friction-free environment to measure the drag exerted on the cylinder. The real-time image of the setup is shown in Fig. 3. The air bearings are allowed to move effortlessly when the cylinder is exerted by even a light touch force. By a four-way junction system attached to the tube hanging above the setup, compressed air from the compressor is transmitted to the air bushings through a 19 mm diameter hose. For the best friction-free movement of the air bushings, the pressure was maintained at 6 bar. The air was transferred from the connecting point to the air bushing intakes using four pipes, each measuring 5 mm in diameter. The compressor is an oil-free air compressor with a 35-liter tank and a 2.12-horsepower motor. The dust particles captured by the air compressor were filtered using a polycarbonate air filter regulator combination. Since the moisture was periodically drained, it also worked as a moisture regulator. The regulator's primary function was to supply compressed air for the entire duration of the experiment at a steady pressure. This apparatus for direct drag measurement was inspired by the work of Dewey *et al.* [34] in which the efficiency of flexible panels was measured by direct

thrust and power measurements acquired utilizing air bushings to allow friction-free movement of the apparatus.

A dumbbell-shaped load cell was used to measure forces and to act as a transducer by transforming these forces into electrical signals. The signals were measured using a computer setup. Four strain gauges were coupled in a balanced Wheatstone full bridge arrangement to form the load cell. The magnitude of the drag force with the tapered cylinder and fluid characteristics is anticipated to be relatively low because the current experiments are being conducted in a low Re range. To monitor just the drag and reject extraneous vibrations as noise in the signal, it was necessary to amplify the load caused by drag using the lever arm. A 60 cm  $\times$  5 cm lever arm was designed. It was easier to enhance the force with which the setup impacts the load cell by changing the placement of the lever's hinge. The drag force exerted on the cylinder is amplified and transferred onto the load cell and a corresponding voltage signal is generated as a result. This lever arm is an important part of this apparatus, and this idea was taken from Buchholz *et al.* [35] where the lever arm was used to amplify the forces while measuring the unsteady thrust and propulsive efficiency produced by biologically inspired oscillating hydrodynamic propulsors. Extra care was taken to reduce or eliminate external disturbances because of the sensitivity of the load cell. A few metallic L angles were clamped to a table to prevent the vibrations from the tunnel from also reaching the load cell mount. The air tubes were built to hang on the wall away from the tunnel table, and foam sheets were inserted at the contact points of the tubes with the frame to further dampen the vibrations that the compressor could send through the tubes.

## B. Data processing

The flow uniformity was verified by using both the hot-film anemometry and PIV. The fiber-film sensor was placed at  $x/D = 2$  downstream of the cylinder for estimation of the shedding frequency of the straight cylinder. The spanwise wavelength of modes from the digital images was acquired by drawing out a straight line across the spanwise length and examining the pixel intensity profile along it. FFT (fast Fourier transform) was performed over the pixel intensity profile to find the spanwise wavelength. A windowed (50% overlap) FFT was performed to calculate the instantaneous spanwise wavelength spectrum. The hamming function was applied to each window to decrease the finite length effects. Hot-wire data were taken by traversing the fiber-film probe by 100 mm in steps of 1 mm in the  $y$  direction with the help of the traverse for finding the wake-frequency response in the spanwise ( $x$ - $y$ ) plane. The repeatability of the frequency responses provided insight into the spanwise wavelength of the various modes.

## C. Validation

The reliability of the experimental setup was examined by reproducing a few established flow phenomena of rotating straight cylinders. Validation of the three-dimensional modes in the wake of a rotating straight cylinder was checked. The present results were compared with the study of Radi *et al.* [19] and the results are found to be similar. In Fig. 4 the flow visualization of mode F is compared and presented. The spanwise structures of mode F originated from the surface of the rotating cylinder, at  $Re = 275$ ,  $\alpha = 2.3$  where  $\alpha$  is the ratio of the surface velocity of the cylinder to the free stream velocity. Bright streak lines are created when the hydrogen bubbles cross the laser sheet. The average spanwise wavelength of mode F found from the spectral analysis is  $\lambda/D = 0.5$ .

The variation of coefficient of drag for a straight circular cylinder with the Reynolds number is shown in Fig. 5 to validate the current experimental setup for direct drag measurement. To assess the reliability of the setup, the current experimental data for a circular cylinder were compared with those of Weiselberger [36], Zdrakovich [37], and Bosch and Guterres [38]. The values revealed a trend that was consistent with the literature; however, the values were overestimated by 2% to 8%. The torque augmentation caused by the weight of the lever arm relative to its hinge point may be the reason for this overestimation of values.

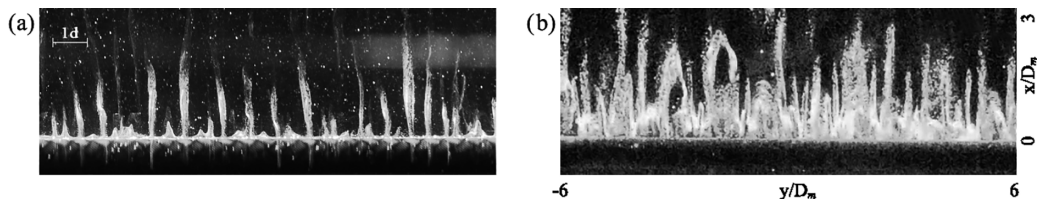


FIG. 4. Validation for spanwise flow visualization with the data of (a) Radi *et al.* [19] and (b) the present experiment with a rotating straight cylinder. The flow is directed from bottom to top at  $Re = 275$  and  $\alpha = 2.3$ . The scaling is the same for both images. The sense of rotation is such that the cylinder surface seen by the reader is moving toward the top of the frame.

### III. RESULTS

Flow visualizations, hot-film measurements, and PIV data at  $Re_{\text{mean}} = 250$ , with subsequent qualitative and quantitative analysis, constitute the experimental results and are presented here. In this section, the behavior of the cylinder wake structure with variation of oscillation amplitude and forcing frequency will be discussed. The effect of forcing frequency on the drag coefficient at various oscillation amplitudes will also be presented.

#### A. Hydrogen bubble flow visualization of spanwise vortices

The spanwise wake structure behind a cylinder executing rotary oscillations at various oscillation amplitudes and FR is shown in Fig. 6. The platinum wire is  $1D_m$  upstream in all the images and is marked by a red arrow in the image where the stationary cylinder wake is shown. In the present experiments, oblique shedding ceases and parallel shedding begins near  $FR = 0.75$  for all the oscillation amplitudes observed in the present experiment. Williamson [6] reported the phenomenon of oblique vortex shedding at a low Reynolds number ( $64 \leq Re \leq 180$ ) for a stationary straight cylinder wake. The change in oblique shedding modes was attributed to the Strouhal discontinuity. This is because of a transition from a situation in which the central flow over the span matches the end boundary conditions to a situation in which the central flow cannot match the end conditions. Due to the presence of spanwise cells with different frequencies, quasiperiodic spectra of velocity fluctuations are observed in the second case. It was also observed that the convection velocity

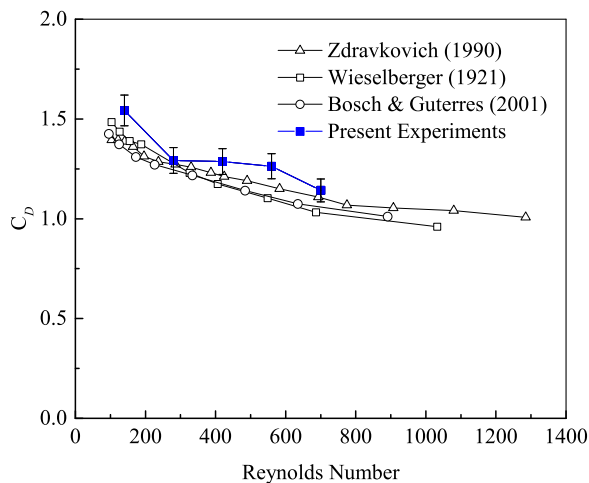


FIG. 5. Coefficient of drag vs Reynolds number for a straight circular cylinder.

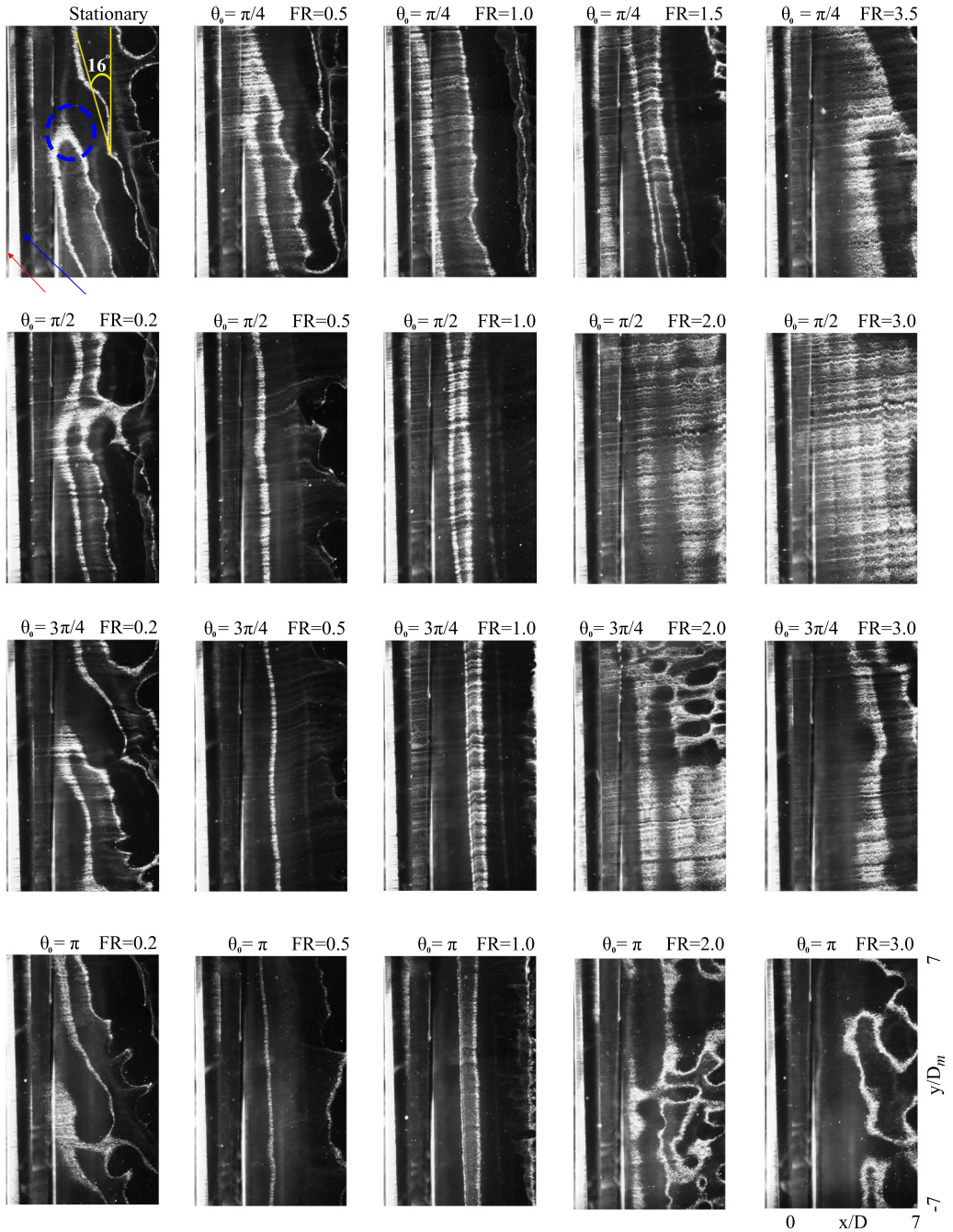


FIG. 6. Three-dimensional spanwise structures in wake of rotationally oscillating tapered cylinder (taper ratio of 70:1) at various oscillation amplitudes and forcing frequencies at  $Re = 250$ . Flow is directed from left to right, and the scaling is the same for all the images. The cylinder is marked by a blue arrow, and the platinum wire is marked by a red arrow in the image where the stationary cylinder wake is shown.

remains almost unchanged between oblique and parallel shedding, at a given  $Re$ . The convection velocity would be low where the three-dimensionalities in the wake are observed because of less downstream distance, and the subtraction of convective velocities may result in stationary vortices [39]. Techet *et al.* [18], by PIV, showed that three-dimensional spanwise vortices are identified in convective velocity subtracted flow. Vortex dislocations are observed at times when vortices in adjacent spanwise positions move out of phase with one another. Ahmed [40] found that vortex dislocation occurs when a strained vortex undergoes axial compression. The present work demonstrates that this characteristic of the wake and spanwise structures is affected by the cylinder's rotational oscillation.

Figure 6 shows that at low forcing frequencies ( $FR = 0.2$ ) and all forcing amplitudes vortex splitting occurs similar to the case of a stationary tapered cylinder. The vortex splitting is denoted by a blue circle in the figure where the wake of a stationary cylinder is shown. Spanwise disturbances are visible at low forcing frequencies, similar to stationary cylinders. In the present study, three-dimensional vortex splitting refers to an entire splitting process involving multiple small-scale vortices that can be observed simultaneously. Eisenlohr and Eckelmann [41] demonstrated that vortex splitting takes place because the shedding frequency from a bluff body is not necessarily uniform across the wake's entire span. Vortex splitting takes place when the oblique angle is too high (observed over  $20^\circ$ , more frequently above  $30^\circ$ ). Additionally, when the axes become excessively curved, the subsequent axis forms by omitting a vortex that extends partially across the spanwise region. To maintain circulation conservation, the extra vortex must either short circuit with the vortex on the far side of the vortex street, as suggested by Gerrard [42], or divide its circulation among its nearest neighbors, or a combination of the two. Nevertheless, vortex splitting can be controlled by adjusting the forcing parameters. Figure 6 shows that at  $FR = 1$ , vortex splitting is controlled and the flow eventually turns parallel for all oscillation amplitudes. The angle of oblique shedding between vortex axes and cylinder axis varies between about  $15^\circ$  and  $30^\circ$  for a stationary circular cylinder wake among a majority of researchers. In the present experiment with a tapered cylinder, oblique shedding of  $16^\circ$  is marked in Fig. 6. The effect of forcing frequencies on the wake of a rotationally oscillating tapered cylinder at various oscillation amplitudes is discussed in the following subsections.

### 1. Effect of $FR$ at $\theta_0 = \pi/4$

For an oscillation amplitude of  $\theta_0 = \pi/4$ , the oblique shedding angle decreases with an increase in forcing frequency up to  $FR = 1$  where the shedding becomes almost parallel. With a further increase in forcing frequency, the oblique shedding resumes and the oblique shedding angle increases with an increase in forcing frequency as seen in Fig. 6 ( $FR = 1.5$ ). At  $FR = 3.5$ , we again observe vortex splitting because of an excessive increase in oblique shedding angle similar to that for a stationary cylinder.

### 2. Effect of $FR$ at $\theta_0 = \pi/2$

For oscillation amplitude of  $\theta_0 = \pi/2$ , as observed in Fig. 6, initial oblique shedding from a stationary cylinder is transformed to parallel shedding at a lower value of  $FR = 0.5$  as compared to the case of  $\pi/4$ . Notably, as the forcing frequency is increased further, no oblique shedding is observed and the flow remains parallel until  $FR = 3.0$ . At  $FR = 2$  and  $FR = 3$ , the downstream wake is nearly two-dimensional with no spanwise perturbations on vertical vortex columns. The vortices appear as a straight timelines parallel to the cylinder axis where they get illuminated by the laser sheet. Parallel shedding of spanwise vortex columns without spanwise perturbations indicates a two-dimensional flow that is coherent with space and time. A possible explanation for this absence of spanwise vortices may be the locking on of the cylinder oscillation frequency with the wake shedding frequency at these  $FR$ s as observed in [25], which (for a circular cylinder) from the end view visualization, at  $Re = 185$  and  $FR \geq 2$ , showed that the hydrogen bubble sheet appeared as a line with no out-of-plane motion, suggesting a two-dimensional flow. This also confirmed, as

suggested by Thiria and Wesfreid [43], that when the wake is locked on, the three-dimensionalities tend to get suppressed. This lack of three-dimensionalities, caused by rotary oscillations in the wake, has a variety of applications, including fluid mixing control and some defense applications [23,44]. This phenomenon may be further justified theoretically by relating it to the consequences of the Taylor-Proudman theorem when observed from a rotating frame of reference attached to the cylinder, which demonstrates that the flow is two-dimensional if the Coriolis force dominates over the inertia and viscous forces [45–47]. The high forcing frequencies at which this forced two-dimensional flow occurs indicate a higher Coriolis force, which further explains the occurrence of this forced two-dimensional flow.

### 3. Effect of FR at $\theta_0=3\pi/4$

The spanwise wake structure for  $FR \leq 2$ , at an oscillation amplitude of  $\theta_0 = 3\pi/4$ , was similar to that of  $\theta_0 = \pi/2$  (as seen in Fig. 6). However, at  $FR = 2$ , cellular shedding is observed at the upper half of the cylinder. A similar type of cellular structure was also observed by Bhattacharyya *et al.* [48] in their study of the interaction of wall boundary layer and vortices in the wake of a rotationally oscillating circular cylinder. This cellular structure was named mode Y, and most of the features found in the spanwise cellular structure of the present study are identical to mode Y. Nevertheless, in the present study, this structure is visible at  $FR = 2$ , whereas in prior research it was visible at  $FR = 2.75$ . In contrast to the study of Bhattacharyya *et al.* [48], in the present investigation, the cellular structure is observed only behind the upper half (i.e., the region of the cylinder with the larger diameter) of the cylinder. The bottom half of the cylinder wake in the present study exhibited a two-dimensional flow. This observation could be attributed to the variation in cylinder diameter and change in the local Re number associated with it or the end conditions. This mode was made visible by movement of the vertical platinum wire along the  $z$  axis; hence, the platinum wire is placed in a location where the three-dimensional patterns are visible. Wire movements of 1 mm in the cross-stream plane made it difficult to observe this mode, which exhibited only slightly perturbed two-dimensional shedding. This may be because the flow is two-dimensional for this FR at other oscillation amplitudes ( $\theta_0 = \pi/2$  and  $\theta_0 = \pi$ ).

### 4. Effect of FR at $\theta_0 = \pi$

At an oscillation amplitude of  $\pi$ , oblique shedding transforms to parallel shedding at  $FR = 0.5$  similar to  $\theta_0 = \pi/2$  and  $\theta_0 = 3\pi/4$ . Three-dimensionalities are reduced to a significant extent for forcing frequency,  $FR = 1$ , like for the case of oscillation amplitude of  $\theta_0 = \pi/2$  and  $\theta_0 = 3\pi/4$ . For forcing frequencies,  $FR \geq 2$ , distorted spanwise structures are observed throughout the span in the wake of the cylinder. A lack of spatial coherence is noticed in the wake, and the spanwise structures were found to be highly random.

### B. Mode Y

Flow structures at  $FR = 2$  and  $\theta_0 = 3\pi/4$  were further studied due to their interesting wake pattern in the spanwise plane [see Fig. 7(a)]. Similar cellular structures observed for a half-span in the present study were observed for the entire span of a straight cylinder at  $FR = 2.75$  by Bhattacharyya *et al.* [48]. These cells are distinguished by oval voids (cells) and hydrogen bubbles that curl toward the voids. With increasing downstream distance, the cells become flatter and the structures are repeatable. It is interesting to note that this mode occurs in the vicinity of two-dimensional parameter space (forcing frequency and amplitude) where the flow is two-dimensional (seen in Fig. 6). This mode of shedding was termed mode Y. For a tapered cylinder, mode Y occurs such that the cells are observed in the upper half of the cylinder (larger diameter side) and the flow is two-dimensional at the lower half [see Fig. 7(a)]. Gaster [3] showed that the signal produced by a hot wire in the flow past a straight stationary cylinder was almost periodic, but for a tapered cylinder the signals revealed increasing amounts of low-frequency content and randomness with an

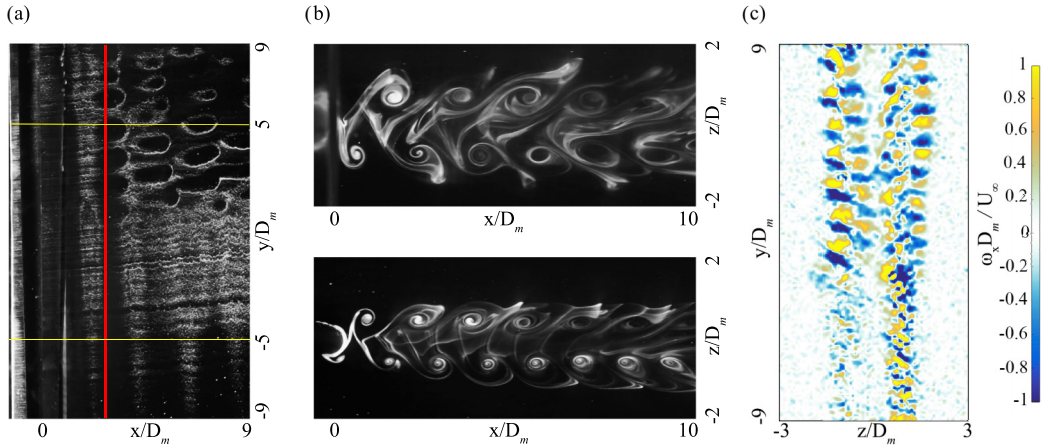


FIG. 7. Mode Y at  $\theta_0=3\pi/4$  and  $FR = 2$ . (a) Hydrogen bubble flow visualization in the  $x$ - $y$  plane. The platinum wire is  $1D_m$  upstream of the cylinder. (b) Laser-induced fluorescence flow visualization in the  $x$ - $z$  plane (top:  $y/D_m = +5$ ; bottom:  $y/D_m = -5$ ). The yellow lines in (a) denote the plane where the image is taken. (c) PIV data in the  $y$ - $z$  plane. The red line in (a) denotes the plane where the data are taken.

increase in taper. To link the flow characteristics observed in the  $x$ - $y$  plane, LIF flow visualization was performed in the  $x$ - $z$  plane. The locations where these experiments were performed are denoted by yellow lines in Fig. 7(a). The visualization image on top of Fig. 7(b) represents the flow in the  $x$ - $z$  plane at  $y/D_m = 5$  where the cellular structures are observed in the spanwise plane. The observed vortices are not distinct suggesting an out-of-plane motion and the resulting three-dimensionality in the flow. The visualization image at the bottom of Fig. 7(b) represents the flow in the  $x$ - $z$  plane at  $y/D_m = -5$  where the cellular structures are not observed in the spanwise plane and the flow appears two-dimensional (lack of spanwise perturbations) at that location. The vortices are more distinct as compared to the data observed at  $y/D_m = 5$  (upper half), suggesting a lack of out-of-plane motion which results in a lack of three-dimensionality (spanwise perturbations) in the flow. Figure 7(c) shows the results of instantaneous PIV data in the  $y$ - $z$  plane taken simultaneously with the hydrogen bubble flow visualization in the  $x$ - $y$  plane. The location where these PIV data were obtained is shown by a red line in Fig. 7(a). It can be observed that from the top end of the cylinder, where the diameter is greatest, to the bottom end of the cylinder, where the diameter is smallest, the size and strength of the vortices decrease. This was consistent with the hot-wire measurements by Anderson and Szweczyk [49] showing frequency content of a stationary tapered cylinder which showed that the cells at the high velocity or small diameter end of the cylinder produced a narrow-band power spectrum peak which indicated a high degree of two-dimensionality in that region, and the cells at the low velocity or large diameter end of the cylinder produced a more broad-band power spectrum peak which indicated a high degree of three-dimensionality in that region. These PIV data also reveal that the cellular structures observed in the flow visualization experiments are counter-rotating vortices. The average distance between the area wetted centroid of two blue vortices or two yellow vortices in the upper half of the cylinder wake gave us an estimation of the spanwise wavelength. The average spanwise wavelength of this mode was observed to be  $\lambda/D_m \approx 1.5$  ( $\lambda/D \approx 1.6$  was observed for mode Y in the wake of a straight circular cylinder) from the PIV analysis. The spanwise wavelength of mode Y was also verified using spectral analysis of the flow visualization image. For spectral analysis, the pixel intensity was measured across the upper half spanwise length, and an FFT of the intensity profile gave a peak which is an estimate of the spanwise wavelength.

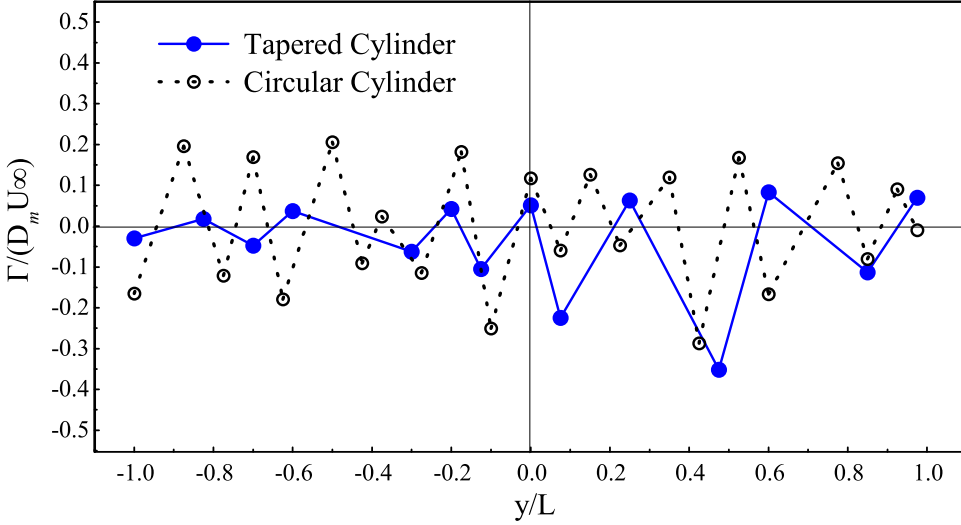


FIG. 8. Spanwise variation of normalized circulation of streamwise vortices for mode Y calculated from the vorticity field in the  $y$ - $z$  plane.  $y/L = 0$  corresponds to the middle of the cylinder wetted length.

The comparison of nondimensional circulation of streamwise vortices in the  $y$ - $z$  plane (at  $x/D = 3$ ) along the span of the cylinder for mode Y of a straight circular cylinder with a diameter of 8 mm and a tapered cylinder with the same mean diameter at  $Re = 250$  is shown in Fig. 8. The circulation was found by acquiring the area integral of vorticity ( $\omega_x$ ) of the streamwise vortices found by PIV. The origin is the spanwise position of the center of the wetted tapered cylinder in the  $y$  direction (where the diameter is 8 mm), the upper extreme of the wetted tapered cylinder (where the diameter is 10 mm) is +1 in the  $y$  axis ( $y/L$ ), and the lower extreme (where the diameter is 6 mm) of the wetted cylinder is  $-1$ . The counter-rotating vortex in the  $y$ - $z$  plane is observed for both the tapered and straight cylinders. For a straight cylinder at  $FR = 2.75$ , the circulation of the vortices is almost constant throughout the span signifying a uniform three-dimensional flow across the entire span, whereas, for a tapered cylinder at  $FR = 2$ , the strength of the counter-rotating vortex decays in the lower half of the span. This is consistent with the study of Anderson and Szewczyk [49] which showed that for a stationary tapered cylinder in a uniform flow, the vorticity shed from the boundary layer decreases across the span with decreasing local diameter to produce a spanwise variation in the strength of the primary vortices. For the straight circular cylinder, the average streamwise ( $y$ - $z$  plane) vortex circulations  $\Gamma_{x_{aver}}/(DU_{\infty})=0.19$  are in good agreement with the studies of Wu *et al.* [50] and are much smaller than the average primary vortex circulations  $\Gamma_{y_{aver}}/(DU_{\infty}) \approx 1.5$ . For mode Y flow conditions of straight circular cylinder, the maximum primary circulation  $\Gamma_{y_{max}}/(DU_{\infty})$  found by Kumar *et al.* [25] at  $FR = 2.75$  was almost four times more than the maximum streamwise circulation  $\Gamma_{x_{max}}/(DU_{\infty})$  found in the present study.

Since the cellular structures were observed partially [see Fig. 9(a)], one of the obvious questions that come up is the dependence of the local Reynolds number on the spanwise structures. It was found that the local Reynolds number (corresponding to local diameter) at  $y/D_m = 9$  was  $\sim 281$ . Hydrogen bubble flow visualization on a straight circular cylinder at  $Re \sim 281$  [see Fig. 9(b)] revealed the formation of spanwise structures at the same forcing conditions ( $\theta_0$  and  $f$ ). This justified the occurrence of the cellular structures at the top half of the tapered cylinder. It must be noted that the same absolute forcing frequency  $f$  was used instead of normalized forcing frequency (FR) because the shedding frequency ( $f_0$ ) changes with  $Re$ , which changes the FR. Coherent structures of mode Y were observed across the span for a flow behind the straight cylinder at  $Re = 250$  [see Fig. 9(c)]. However, at the  $y/D_m=0$ , for a tapered cylinder, the cells were not prominent, which

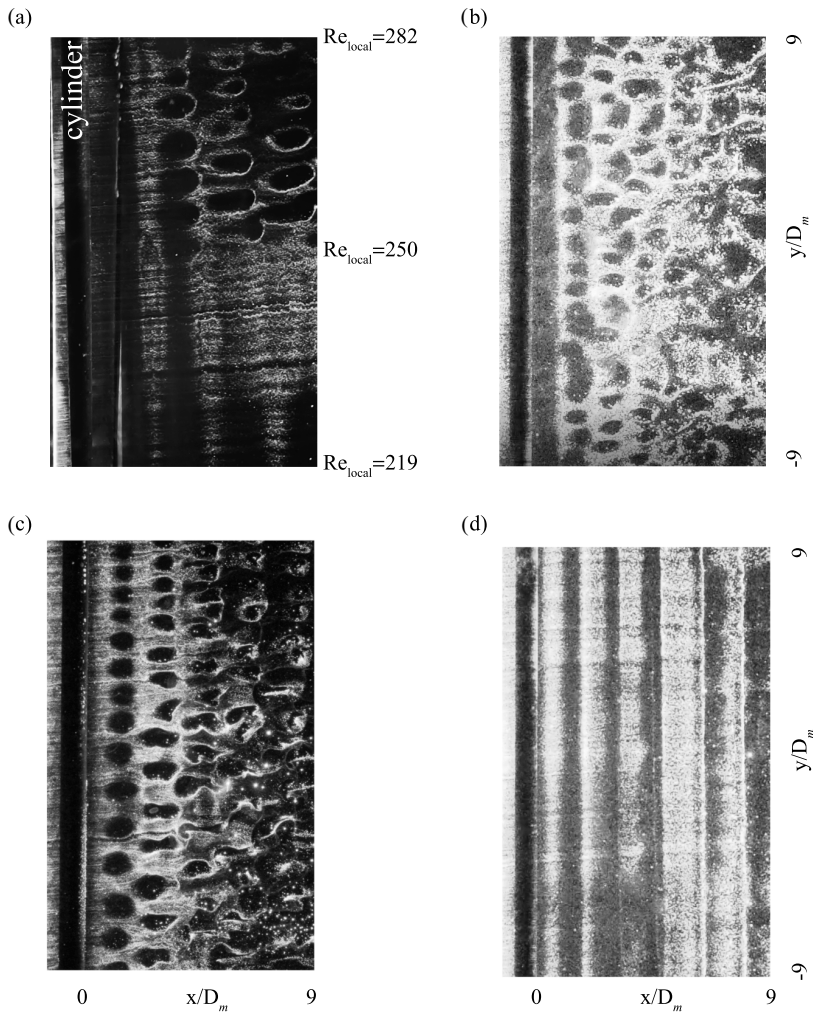


FIG. 9. Hydrogen bubble flow visualization at  $\theta_0 = 3\pi/4$ ; (a) tapered cylinder at  $Re = 250$  and  $FR = 2$ ; (b) straight cylinder at  $Re = 282$ ; (c) straight cylinder at  $Re = 250$ ; (d) straight cylinder at  $Re = 219$ . Scaling is the same for the all the images.

may be attributed to the stronger effect of the two-dimensional flow below. It was found that the local  $Re$  number at  $y/D_m = -9$  was  $\sim 218$ . Flow visualization on a straight cylinder at  $Re \sim 219$  [see Fig. 9(d)] revealed the absence of spanwise structures (no perturbations in the spanwise plane and the vortex columns are perfectly straight) justifying the occurrence of the two-dimensional flow at the bottom half of the tapered cylinder. Another reason for the partial occurrence of the cellular structure may be because these cellular structures were coherently observed for a very small range of forcing parameter space (combination of forcing frequency and amplitude) for a straight cylinder, and this mode occurred in the neighborhood of the forcing parameter space where the flow was two-dimensional. The change in shedding modes across the span of the tapered cylinder was also observed in [18] where at the top (side with larger diameter) 2S mode of shedding was observed, at the bottom (side with a smaller diameter) 2P mode of shedding was observed, and at the middle a hybrid mode of shedding was observed. 2S here refers to a condition where two alternating vortices

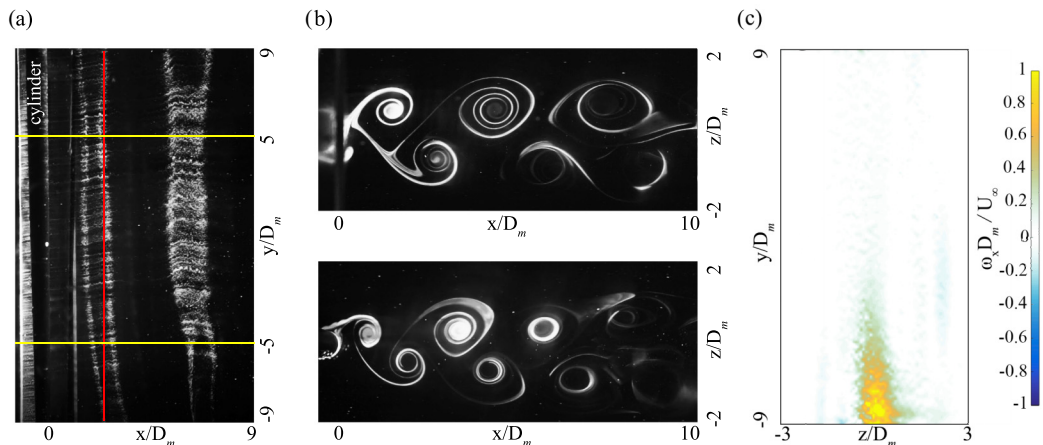


FIG. 10. Two-dimensional flow at  $\theta_0 = \pi/2$  and  $FR = 1$ . (a) Hydrogen bubble flow visualization in the  $x$ - $y$  plane. The platinum wire is  $1D_m$  upstream of the cylinder. (b) Laser-induced fluorescence flow visualization in the  $x$ - $z$  plane (top:  $y/D_m = +5$ ; bottom:  $y/D_m = -5$ ). The yellow lines in Fig. 10(a) denote the plane where the image is taken. (c) PIV data in the  $y$ - $z$  plane. The red line in Fig. 10(a) denotes the plane where the data are taken.

or one pair of alternating vortices are shed per cycle and 2P refers to two pairs of alternating vortices shed per cycle [6].

### C. Forced two-dimensional flow

Certain forcing conditions transform the downstream wake into a two-dimensional state in which spanwise perturbations on vertical vortex columns disappear. The spanwise vortices observed in the wake of stationary tapered cylinders and at low forcing frequencies (for example,  $FR \leq 0.5$ ) disappear at certain forcing parameters. The forced wake becomes two-dimensional and spatially and temporally coherent (less random). This interesting phenomenon is further looked into as the flow conditions affect the drag force on the cylinder. Poncet *et al.* [51] and Jacon *et al.* [52] showed that for a straight circular cylinder the drag coefficient of the three-dimensional flow was  $\sim 14\%$  less than two-dimensional flow and  $\sim 12\%$  more than the forced two-dimensional flow.

A parallel vortex column without spanwise disturbances at  $FR = 1$  and  $\theta_0 = \pi/2$  indicating a two dimensional flow is shown in Fig. 10(a). To link the flow characteristics observed in the  $x$ - $y$  plane, LIF flow visualization was performed in the  $x$ - $z$  plane. The locations ( $y/D_m = \pm 5$ ) where these experiments were performed are denoted by yellow lines in Fig. 10(a). The visualization image on top of Fig. 10(b) represents the flow in the  $x$ - $z$  plane at  $y/D_m = 5$ , and the visualization image on bottom of Fig. 10(b) represents the flow in the  $x$ - $z$  plane at  $y/D_m = -5$ . The images revealed a similar two-dimensional vortex structure without out-of-plane motion in both the top and bottom  $x$ - $z$  planes. Figure 10(c) shows the results of instantaneous PIV data in the  $y$ - $z$  plane taken simultaneously with the hydrogen bubble flow visualization in the  $x$ - $y$  plane of Fig. 10(a). The location ( $x/D_m$ ) where the velocity field in the  $y$ - $z$  plane is taken to understand the distribution of streamwise vorticity by PIV in the  $y$ - $z$  plane is shown by a red line in Fig. 10(a). The origin in the horizontal axis represents the center of the cylinder, while the origin in the vertical axis represents the location of the center of the wetted area in the  $y$  axis. PIV data reveal the absence of counter-rotating vortices found in other three-dimensional cases. This absence of counter-rotating vortices further shows that the flow is two-dimensional. Small periodic disturbances observed in the flow at the bottom end of the cylinder may be because of the bottom wall effect. This end wall effect may be attributed to the large spanwise variation of  $U_\infty/D$  which enhanced three-dimensionality through vortex adhesions

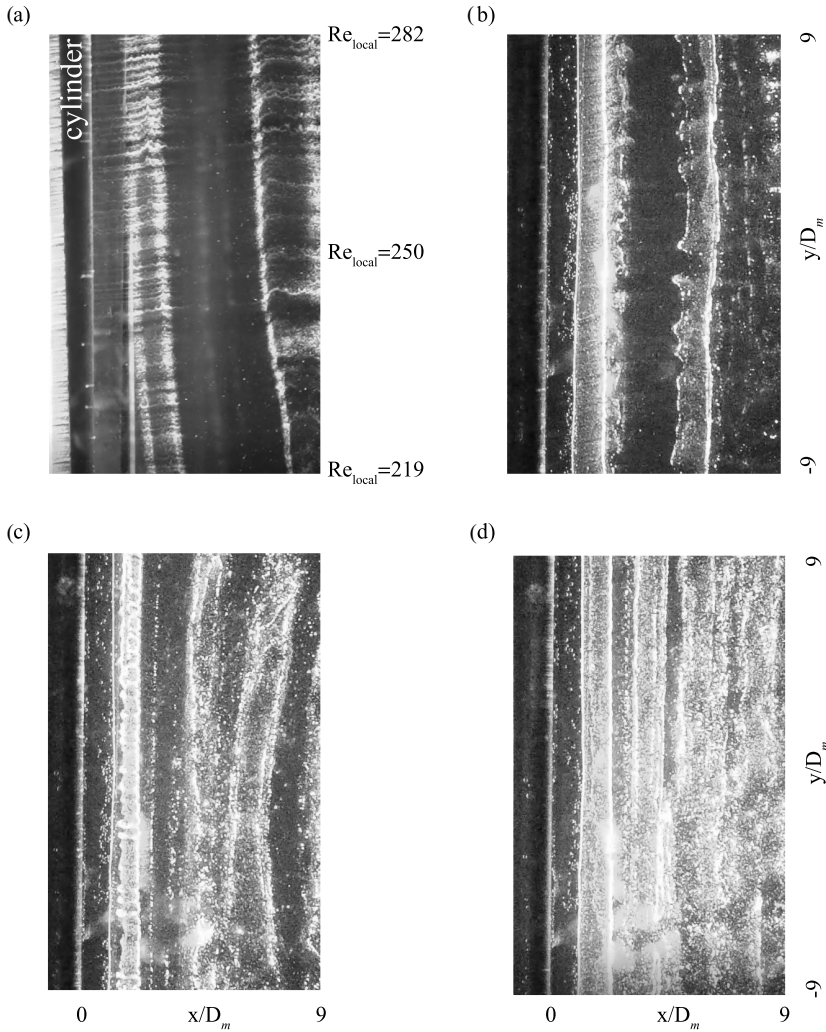


FIG. 11. Hydrogen bubble flow visualization at  $\theta_0 = \pi/2$ ; (a) tapered cylinder at  $Re = 250$  and  $FR = 1$ ; (b) straight circular cylinder at  $Re = 282$ ; (c) straight circular cylinder at  $Re = 250$ ; (d) straight circular cylinder at  $Re = 219$ . Scaling is the same for the all the images.

and dislocations [12]. Silvestrini and Lamballais [53] showed that for a constant diameter circular cylinder sheared inflow may modify the spanwise perturbations and disturbances in the flow.

The effect of the local Reynolds number on the wake structure at  $FR = 1$  and  $\theta_0 = \pi/2$  on the tapered cylinder is shown in Fig. 11(a). Experiments on straight circular cylinders provided interesting information about the flow at these forcing conditions ( $\theta_0$  and  $f$ ). Flow visualization on a straight circular cylinder at  $Re \sim 282$  [see Fig. 9(b)] revealed that although the shedding is parallel, there are perturbations in the spanwise plane, and there is the formation of spanwise structures at the same forcing conditions ( $\theta_0$  and  $f$ ). This showed that the flow is not perfectly two-dimensional at  $Re \sim 282$  and there is an occurrence of the spanwise structures. Even at  $Re = 250$ , the straight circular cylinder exhibited three-dimensional characteristics [see Fig. 11(c)] unlike the tapered cylinder. This three-dimensional mode of shedding for a circular cylinder is observed to become discernible at  $FR = 0.9$  and becomes distinct at  $FR = 1$ . When the forcing frequency is increased

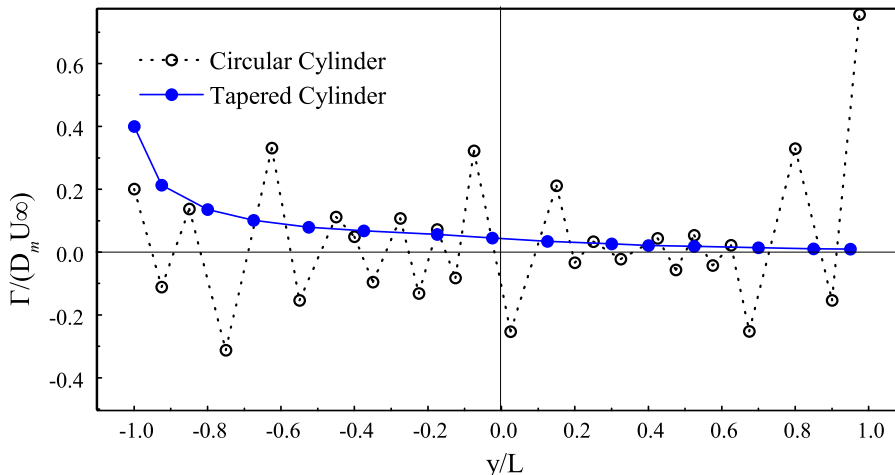


FIG. 12. Spanwise variation of normalized circulation of streamwise vortices at  $FR = 1$  and  $\theta_0 = \pi/2$  calculated from the vorticity field in the  $y$ - $z$  plane using PIV. The origin is the spanwise position of the center of the wetted cylinder along the  $y$  direction, the upper extreme of the wetted cylinder is  $+1$  on the  $x$  axis ( $y/L$ ), and the lower extreme of the wetted cylinder is  $-1$ .

to  $FR = 1.1$ , mode dissociation is observed. Consequently, this mode is observed in a small range of forcing frequency close to  $FR = 1$  where the forcing frequency corresponds to the shedding frequency of the stationary cylinder. Kumar *et al.* [25] also revealed that the instabilities of the wake are very sensitive to the forcing conditions and that even small perturbations in the amplitude can cause the flow to choose one mode over the other. The reason for this shedding mode not being observed for a tapered cylinder could perhaps be due to the changes in the local Reynolds number along the span which in turn changes the local shedding frequency and hence the  $FR$  at that particular location. At  $Re = 219$ , the shedding for a straight circular cylinder was found to be two-dimensional [see Fig. 11(d)] without any spanwise perturbations unlike at  $Re = 282$  and  $Re = 250$ . This may justify the two-dimensional flow behind the tapered cylinder as the two-dimensional flow at the bottom of the cylinder may dominate the flow and cause the entire spanwise vortex column to be two-dimensional. For higher forcing frequencies ( $FR = 2$  and  $3$ ), both the tapered cylinder (shown in Fig. 6) and the straight circular cylinder (not shown here) had a similar wake structure. The flow was two-dimensional without any spanwise perturbation of the vortex column.

The strength of vortices in the spanwise plane would help in understanding the extent of three-dimensionality in the flow. The normalized circulation of the streamwise vortices in the  $y$ - $z$  plane ( $x/D = 3$ ) along the span of a tapered cylinder and a straight circular cylinder for an amplitude of  $\theta_0 = \pi/2$  at a forcing frequency of  $FR = 1$  is shown in Fig. 12. The circulation in the plot for the tapered cylinder shows the lack of counter-rotating vortices (weak three-dimensional vortices) in the  $y$ - $z$  plane. This also justifies the PIV data in the  $x$ - $z$  plane shown in Fig. 10(c). The circulation of the vortices for the tapered cylinder being smaller in magnitude signifies the turning of the flow to two-dimensional. The average streamwise vortex circulations  $\Gamma_{x_{aver}}/(DU_\infty) \sim 0.07$  are much smaller than the average primary vortex circulations  $\Gamma_{y_{aver}}/(DU_\infty) \approx 2$  in the  $x$ - $z$  plane as reported [25] for  $FR = 1$  for a straight circular cylinder. For a straight circular cylinder, the maximum circulation  $\Gamma_{y_{max}}/(DU_\infty)$  found [25] was almost ten times more than  $\Gamma_{x_{max}}/(DU_\infty)$  found in the present work, further showing that the flow is two-dimensional. However, at the bottom end of the tapered cylinder, there were vortices of the same sign which might be due to end effects [also seen in Fig. 10(c)], showing some significant values of normalized circulation. For a straight circular cylinder, significant values of normalized circulation were obtained confirming the presence of counter-rotating vortices in the  $y$ - $z$  plane. This also justified the braidlike three-dimensional

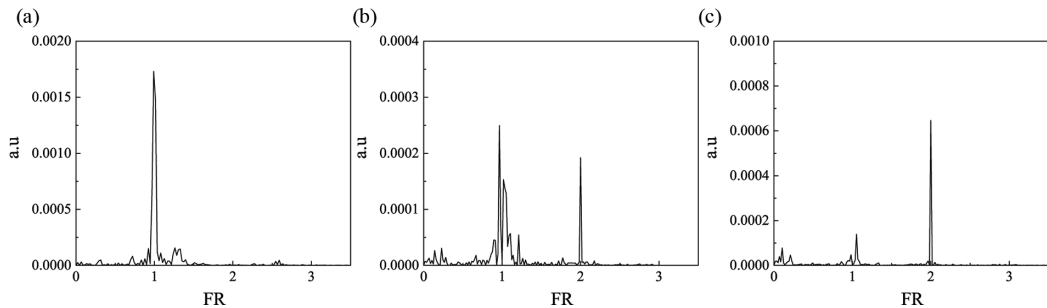


FIG. 13. Frequency response of the wake from hot film anemometry (a) FR = 1,  $\theta_0 = \pi/2$ ,  $y/D_m = 0$ ; (b) FR = 2,  $\theta_0 = 3\pi/4$ ,  $y/D_m = 8$ ; (c) FR = 2,  $\theta_0 = 3\pi/4$ ,  $y/D_m = -8$ .

instabilities found at FR = 1 for the straight circular cylinder as shown in the flow visualization result in Fig. 11(c).

#### D. Spectral content of the wake

Hot-film measurements were taken with a fiber film probe for measuring the frequency content of the wake at a downstream distance of  $x/D_m=2$  at every 1 mm interval in a spanwise direction ( $y$  direction) for 100 mm. These quantitative measurements were done to compare the visual observations in the spanwise plane. Figure 13(a) shows the hot-film data taken at  $y/D_m = 0$ , FR = 1, and  $\theta_0 = \pi/2$  where there is a lack of spanwise perturbation in the flow [the flow is almost two-dimensional as seen in Fig. 11(a)]. The spectrum shows that the wake is having a lock-on phenomenon as the forcing frequency of the oscillating tapered cylinder matches the frequency of the wake. Similar results were found in the study of Bhattacharyya *et al.* [48] for the case when the shedding frequency of the stationary cylinder matched the forcing frequency of the oscillating straight cylinder (FR = 1).

Hot-film analysis shown in Fig. 13(b) revealed the wake at FR = 2 and  $\theta_0 = 3\pi/4$  at a location of  $y/D_m = +8$  [upper half of the cylinder where cellular structures are observed in flow visualization data of Fig. 9(a)] still responds to the cylinder oscillation frequency, but there are clear indications of multiple frequencies present, suggesting complex behavior of this mode. This also suggests that the wake supports a new spanwise mode [consistent with flow visualization data shown in Fig. 9(a)] on the upper half of the cylinder because the dominant frequency is not the forcing frequency at this spanwise location. The spectrum at  $y/D_m = -8$  in Fig. 13(c), shows that the wake is having a lock-on phenomenon as the forcing frequency of the oscillating tapered cylinder matches the frequency of the wake and the forcing frequency is also the dominating frequency. A similar observation is seen for a two-dimensional forced flow at FR = 1 and  $\theta_0 = \pi/2$  which also suggests that the flow at the bottom half of the cylinder is almost two-dimensional and lacks spanwise perturbations. These measurements also confirm the flow visualization data shown in Fig. 9(a) where a two-dimensional flow is seen at the bottom half of the cylinder wake at similar forcing conditions.

#### E. Lock-on parameter space

The lock-on phenomenon, where the cylinder oscillation frequency equals wake shedding frequency was first studied numerically by Okama *et al.* [54] for a rotationally oscillating straight circular cylinder. In the present work, the lock-on parameter space was derived from the spectrum of streamwise velocity fluctuations at a downstream distance of  $x = 2D_m$  from the cylinder and at various forcing parameters using hot-film anemometry. The fiber-film probe was kept at the center of the vertical extent of the cylinder (at  $D_m = 8$  mm) and at  $0.9D$  away from the cylinder center line on the  $z$  axis. Figure 14 illustrates the lock-on parameter space in the amplitude-forcing

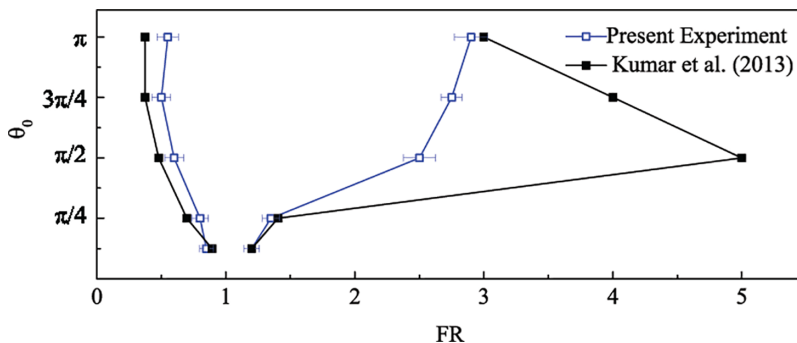


FIG. 14. Lock-on diagram: regions exhibiting lock-on in the amplitude-frequency plane at  $x = 2D_m$  downstream. Five discrete amplitude data points are connected by straight lines to illustrate the parameter space of lock-on.

plane. The figure shows, for each amplitude, the lower and higher limits of the region of forcing frequencies where the dominant downstream near-wake frequency matches the oscillation frequency of the cylinder. The present results are similar to the published literature [25] for a straight circular cylinder at  $Re = 190$ . It is observed from Fig. 17 that the lock-on region depends on both the forcing frequency and the oscillation amplitude of the cylinder. The change in the shedding structure of the vortices as seen in the flow visualization results with the change in forcing parameters is the reason for the difference in the lock-on parameter space. Thiria *et al.* [43] showed that these differences in lock-on ranges were a result of changes in mean flow stability characteristics near the straight circular cylinder. It was seen that the lock-on parameter space decreases with decreasing oscillation amplitude (see Fig. 14) for a tapered cylinder. In addition, for high oscillation amplitudes like  $\theta_0 = \pi$ , the lock-on phenomenon was observed for a wider range of FRs as compared to lower oscillation amplitude. Mahfouz and Badr [55] demonstrated that below a particular forcing amplitude, the lock-on region entirely diminishes. The forcing frequencies at lock-on initiation were found to be similar for both cases of the straight cylinder and the tapered cylinder. The tapered cylinder exhibited the lock-on initiation only at a slightly higher forcing frequency. There was a difference in the termination frequency of lock-on for a straight cylinder [25] and a tapered cylinder for oscillation amplitudes  $\theta_0 \geq \pi/2$ . For the present experiment, there was an absence of an abrupt increase in the termination forcing frequency of lock-on at an oscillation amplitude of  $\theta_0 = \pi/2$ , and the termination forcing frequency of lock-on gradually increased with an increase in oscillation amplitude. Kumar *et al.* [25] also showed that the lock-on parameter space may change at different downstream locations. The errors in the range of FR at which lock-on occurs for a particular oscillation amplitude is less than 3%. These errors may arise due to change in shedding modes when lock-on is initiated or terminated. This lock-on parameter space is essential for analyzing the variations in drag coefficients obtained for different forcing frequencies and oscillation amplitudes.

#### F. Drag analysis with direct drag measurement setup

Direct drag measurement of the drag force on tapered cylinder was done using the setup described in Sec. II A 4. The load cells were calibrated using a variety of known weights in order to determine the slope between the load applied to the load cell (mN) and the potential difference (mV) observed across the imbalanced Wheatstone bridge. The slope derived from the potential difference data is then used to compute the actual drag force applied to the cylinder throughout the experiment. A direct method of calibration was used, in which the load cell was placed in the setup in its position, and weights were added to the setup by means of a pulley. With regard to the load cell measurement, the aim was to take into account all possible setup effects, such as friction, tension in the tubes, the gravity component of the sloped arrangement, etc. As the weights are added gradually, the hanger

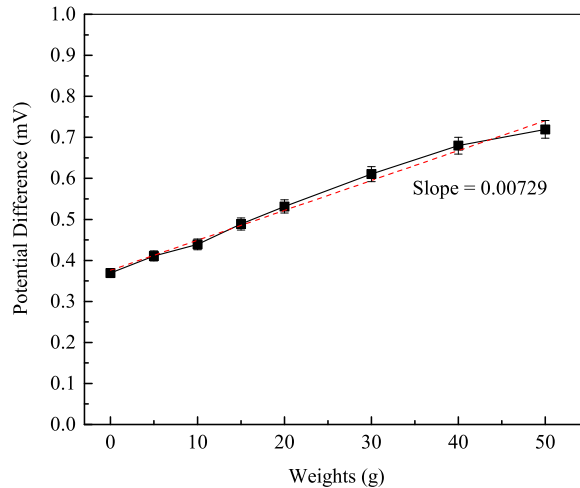


FIG. 15. Calibration of 1 kg capacity load cell at 1:11 lever arm ratio.

component pulls the setup via a pulley system, pressing the load cell and producing the correct deflection in the load cell. For the amplification of the forces, the calibration was done at a lever arm ratio of 1:11. Weights up to 50 grams were employed at this lever arm ratio, producing a linear slope of 0.0073 mV/mN. (Fig. 15). The effective drag force was the difference between the drag force obtained at a specific Reynolds number and the drag force obtained without any flow in the water tunnel. The coefficient of drag from the effective drag force  $F_D$  was obtained by

$$C_D = \frac{F_D}{\frac{1}{2}\rho U_\infty^2 S}, \quad (4)$$

where  $\rho$  is the water density and  $S$  is the frontal area of the cylinder.

Figure 16 shows the comparison of drag coefficients of tapered and straight cylinders at various Reynolds numbers. Except for a Reynolds number of 150, when the difference was roughly 20%, it was found that the drag coefficient for the tapered cylinder was about 10% lower than the straight

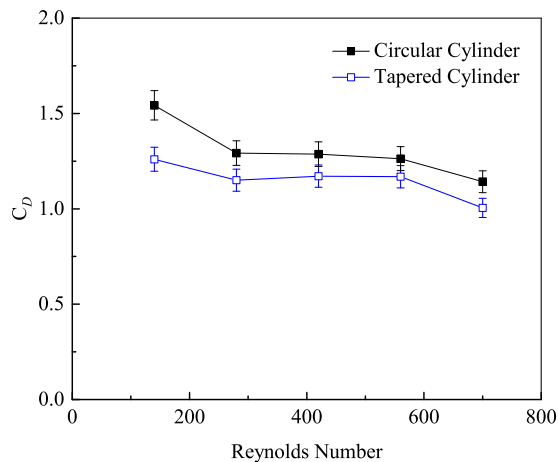


FIG. 16. Comparison of  $C_D$  for a stationary tapered cylinder with a stationary straight circular cylinder at various Reynolds number.

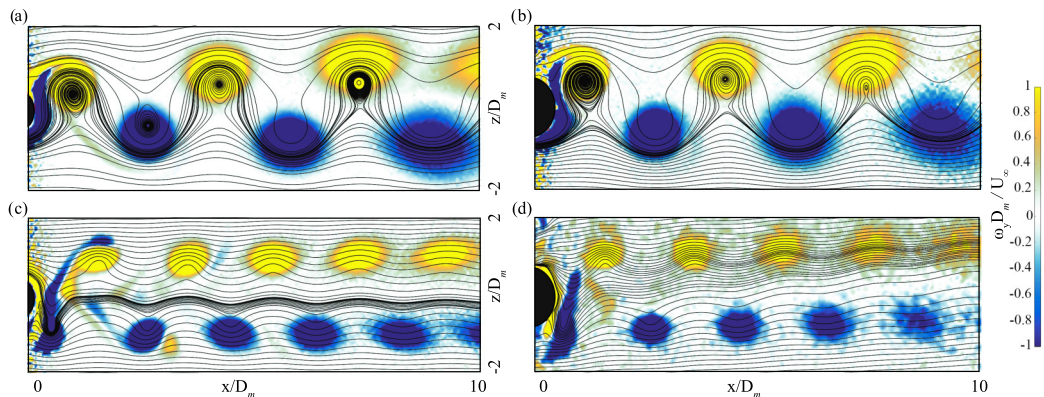


FIG. 17. Vorticity from the velocity field obtain by phase-locked time-averaged PIV (a) at  $FR = 1$  and  $\theta_0 = \pi/2$  at  $y/D_m = -5$ ; (b) at  $FR = 1$  and  $\theta_0 = \pi/2$  at  $y/D_m = +5$ ; (c) at  $FR = 2$  and  $\theta_0 = 3\pi/4$  at  $y/D_m = -5$ ; (d) at  $FR = 2$  and  $\theta_0 = 3\pi/4$  at  $y/D_m = +5$ .

cylinder. These results confirm the observation of Bosch and Guterres [38] for a cylinder with a taper ratio of 60 (at a higher Reynolds number of  $1200 \leq Re \leq 10\,000$ ) where the drag coefficients for a tapered cylinder were lower by 10%–15% than a straight cylinder. Because of the geometry of the tapered cylinder, this occurrence could be a result of the three-dimensional effects. The results were also consistent with the study of Gaster [3] at  $5000 \leq Re \leq 50\,000$ , where, compared to the straight cylinder at a similar Reynolds number, the taper substantially reduced the sectional drag coefficient by up to 20% and produced significant spectral broadening. Gaster suggested that the reason for this decrease in drag was spectral broadening, which was essential if the vortices were to maintain any spanwise coherence. The drag coefficient at  $Re = 250$  for a stationary straight circular cylinder was observed to be 1.48, and the drag coefficient at  $Re_{\text{mean}} = 250$  for a tapered cylinder was found to be 1.28 ( $\sim 13\%$  less than the straight circular cylinder). The experimental errors in direct drag measurements were less than 5%. The drag of a rotationally oscillating tapered cylinder was not obtained with the help of this setup due to the complications arising from the vibrations of the setup because of rotational oscillations. To approximately obtain the drag of the rotationally oscillating tapered cylinder, planar PIV was conducted, which will be discussed in the next section.

### G. Drag analysis with PIV

The data on velocity fields obtained from PIV is used to extract velocity profiles which are used to obtain estimates of drag coefficient. To check the reliability of the PIV setup, vorticity fields from the velocity data in the  $x$ - $z$  plane obtained by phase-locked rime averaged PIV as seen in Fig. 17 were compared with the flow visualization results in the  $x$ - $z$  plane. Figures 17(a) and 17(b) revealed alternating vortices which showed good similarity with the flow visualization results under similar forcing conditions [see Fig. 10(b)]. Similarly, Figs. 17(c) and 17(d) corresponding to the flow at  $FR = 2$  and  $\theta_0 = 3\pi/4$ , exhibited a high degree of resemblance to the flow visualization results under comparable forcing conditions [see Fig. 7(b)]. The sectional drag coefficient obtained at  $y/D_m = -0.5, 0, \text{ and } 0.5$  is found to be approximately the same, hence, the sectional drag was considered to be the global drag according to Eq. (2). PIV for drag analysis was performed at the two-dimensional ( $x$ - $z$ ) plane at  $y/D_m = 0$ . The drag coefficient value for a stationary cylinder at this location is approximately similar to the value obtained by direct drag measurement (shown in Fig. 19). It must be noted that this is an approximate estimate as an assumption made for drag prediction by PIV is that the flow is two-dimensional (in the  $x$ - $z$  plane at the center of the cylinder wetted area), which strictly is not true since forcing and tapering greatly alter the flow in the third dimension depending on the forcing frequency and amplitude.

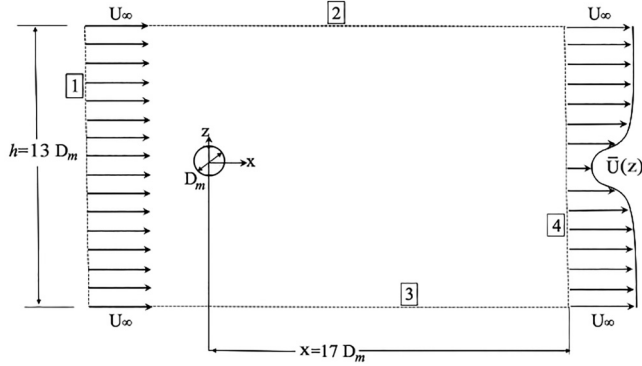


FIG. 18. Schematic of control volume specification for drag calculation. The control surfaces 1, 2, and 3 are assumed to possess  $U_\infty$  value.

The momentum deficit term in Eq. (1) is sufficient to calculate the drag coefficient in the far wake using the mean velocity profile as the static pressure is almost recovered to its free-stream value here. If the velocity profiles are taken  $\approx 30D_m$  downstream from the cylinder, the contribution of the second term can be neglected [27]. However, in the present PIV setup, the visualized downstream distance is limited ( $17D_m$ ). Hence, the estimation of momentum deficit and turbulence terms in the near downstream location is important. The domain size and the free-stream velocity value were kept constant for all the cases considered to have consistency in the results. A streamwise domain extent of  $x/D_m = 16$  and  $15$  also yielded approximately same values of drag coefficient ( $\pm 2\%$  from the  $C_D$  values obtained from a streamwise domain of  $x/D_m = 17$ ) under similar forcing conditions. The resulting values from the present analysis are approximate estimates; however, they would provide a trend of the functional dependence of drag on the forcing parameters. Figure 18 shows the schematic of the control volume used for drag calculation. The control surfaces labeled 2 and 3 are assumed to have a constant velocity value, and because of the absence of data in the upstream

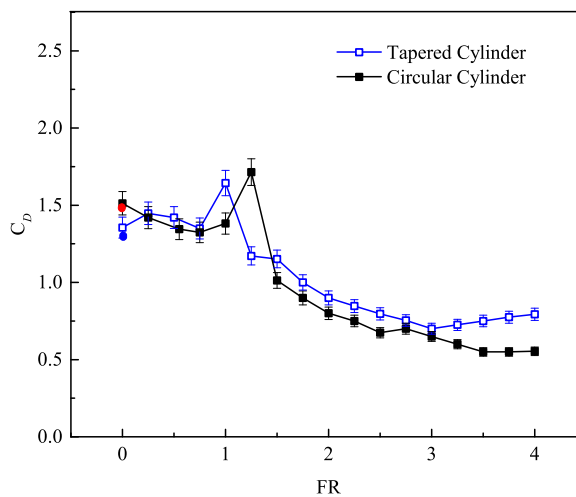


FIG. 19. Variation of drag coefficient with forcing frequency at  $\theta_0 = \pi/2$  for a straight circular cylinder and tapered cylinder. The red dot signifies the  $C_D$  value obtained for a stationary straight circular cylinder, and the blue dot signifies the  $C_D$  value obtained for a stationary tapered cylinder by direct drag measurement.

region, the edge containing the cylinder was considered as the free stream region with a constant  $U_\infty$  value for all the calculations.

The drag coefficient obtained for a stationary circular cylinder with PIV was  $C_D = 1.51$ , and the drag coefficient obtained for a stationary tapered cylinder with PIV was  $C_D = 1.34$ , which is consistent with the values obtained by direct drag measurement. The distribution of drag coefficient at various forcing frequencies at an oscillation amplitude of  $\theta_0 = \pi/2$  is illustrated in Fig. 19. The present study validates the theory of Wu *et al.* [56] that the drag coefficient can be reduced below its steady-state magnitude when there is a frequency mismatch which is observed for forcing frequencies less than the lock-on initiation FR values. For a tapered cylinder, the reduction of drag was  $\sim 15\%$  at forcing frequencies below the lock-on initiation forcing frequency. The peak in the drag coefficient plot occurs at  $FR \sim 1$ , just after the initiation of the lock-on phenomenon in the tapered cylinder. One of the reasons for this occurrence may be attributed to the fact that after lock-on occurs, the vortices formed in the vicinity of the cylinder are stronger with higher suction pressure. This occurrence confirms the experimental findings of Okama *et al.* [54] and computational findings of Cheng *et al.* [57]. When the flow enters the lock-on regime, there is constructive interference (the first shed vortex rotates in the opposite direction of the cylinder's motion) up to a certain forcing frequency where the  $C_D$  reaches its local maxima. This analogy of constructive and destructive interference is described in the experimental findings of Thiria *et al.* [24]. With a further increase in forcing frequency, after the maximum  $C_D$  value is attained, we see a considerable decrease in the drag coefficient for both the cases of a straight circular and a tapered cylinder (see Fig. 19). This may be due to the change of the shedding mode ( $x$ - $z$  plane) from Kármán vortices to double vortex shedding mode in which there is destructive interference where the first shed vortex rotates in the same direction as the cylinder's motion for half of the half-period (time from the vortex origination in the one side of the cylinder to the origination of another in the other side of the cylinder in the  $x$ - $z$  plane). At  $FR \geq 1.5$ , the drag coefficient values are observed to be less for a straight circular cylinder than a tapered cylinder, unlike the stationary cases, which may be because of the different shedding modes observed at different forcing conditions. Changing the forcing parameters of the cylinder can make the wake pick one mode over the other. At  $FR = 3$ , a further decrease in the drag coefficient is observed for a tapered cylinder. This may be because of the combined effect of a mismatch of frequency between the tapered cylinder and the downstream wake (out of lock-on parameter space) along with the destructive interference caused by the cylinder on the wake. At  $FR \geq 3$ , the drag coefficients for a straight circular cylinder are observed to be less than that of a tapered cylinder, which may be because of the spanwise variation of the Re number for a tapered cylinder. The uncertainty in drag estimation may also be attributed to uncertainty in particle displacement estimates, which may be due to a bias error and a random error. Bias error is caused because of PIV evaluation algorithm, while random error arises because of measurement uncertainty.

Comparison of Fig. 19 (at oscillation amplitude  $\theta_0 = \pi/2$ ) with Fig. 20 (at oscillation amplitude  $\theta_0 = 3\pi/4$ ) shows that the maximum drag coefficient increases with increasing oscillation amplitude. As seen in the lock-on diagram of Fig. 14, it is observed that for a tapered cylinder as the amplitude increases, the FR parameter space of the lock-on increases. Consequently, the lock-on is initiated at a lower value of forcing frequency as the oscillation amplitude increases. With a decrease in forcing frequency, the time required for vortex formation in the lock-on range at a fixed amplitude increases, which may result in an increase in vorticity fed to downstream vortices. The locked-on vortices become stronger as the amplitude of oscillation increases, as the vorticity generated by the oscillating cylinder is fed to the vortices, resulting in a higher drag peak at a higher amplitude. When the forcing frequency exceeds the termination forcing frequency of the lock-on range, the drag coefficients decrease with increasing forcing frequency. Figures 19 and 20 show that with an increase in the amplitude of oscillation, the decrease in the drag coefficient becomes more prominent. This may be because the convective instabilities decrease as we move beyond the lock-on zone [43].

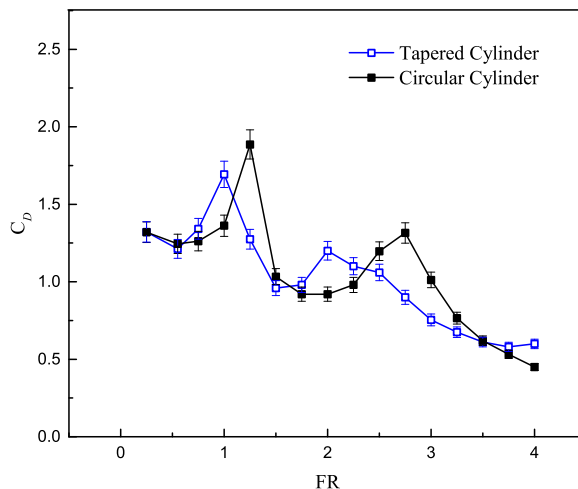


FIG. 20. Variation of drag coefficient with forcing frequency at  $\theta_0 = 3\pi/4$  for a straight circular cylinder and tapered cylinder.

An important observation at  $FR \approx 2$  and  $\theta_0 = 3\pi/4$  for a tapered cylinder, and at  $FR \approx 2.75$  and  $\theta_0 = 3\pi/4$  for a straight circular cylinder, from Fig. 20 shows that for both cases there is an increase in drag coefficient ( $C_D$ ). It is seen that the increase in drag coefficient is more for a straight circular cylinder than for a tapered cylinder. This spike occurs may be because of the three-dimensional mode (mode Y) at these forcing conditions. The spike in the drag coefficient for a tapered cylinder is less may be because of the partial occurrence of mode Y on the upper half and forced two-dimensional flow at the bottom half of the cylinder wake (as seen in Fig. 6) unlike a straight circular cylinder where mode Y is observed across the entire span. This further justifies the findings of Poncet *et al.* [51] and Jacon *et al.* [52] that the drag coefficient of the three-dimensional flow was  $\sim 14\%$  less than two-dimensional flow and  $\sim 12\%$  more than the forced two-dimensional flow.

#### IV. CONCLUSION

Spanwise structures emerging from the flow past a rotationally oscillating tapered cylinder are experimentally studied at  $Re_{\text{mean}}=250$  using the hydrogen bubble flow visualization technique and particle image velocimetry. Laser-induced fluorescence data in the cross-stream ( $x$ - $z$ ) plane were acquired to link the flow fields in the wake cross section ( $x$ - $z$  plane) to visual observations in the  $x$ - $y$  plane. The direct drag measurement technique was used to obtain the coefficient of drag for the stationary cases at various Reynolds number. PIV provided quantitative information about the flow in terms of the streamwise vorticity variation along the span and the drag coefficient at various forcing parameters. These studies helped in quantifying the counter-rotating vortices and the circulation along the span of the cylinder. The lock-on region obtained by hot-film anemometry was mapped using forcing parameter space. The findings of the study include the following:

(1) Visualization data revealed that at a forcing frequency of  $FR = 1$  the oblique shedding in the spanwise plane of a stationary cylinder changes to parallel shedding irrespective of changes in oscillation amplitude.

(2) The forcing parameters ( $\theta_0$  and  $FR$ ) for which the flow was converted from three-dimensional to two-dimensional were found from visualization data, and the same was confirmed by PIV (for example, at  $FR=1$  and  $\theta_0 = \pi/2$ ).

(3) At the upper half of the cylinder wake, the flow resembled a cellular gridlike three-dimensional mode with a spanwise wavelength of  $\lambda/D_m = 1.6$ . This was observed at a forcing frequency,  $FR = 2$ , and oscillation amplitude of  $\theta_0 = 3\pi/4$ .

(4) The strength of circulation of spanwise vortices weakens as we move from the larger diameter end to the smaller diameter end of the cylinder. Frequency content of the wake measured by hot-film anemometry showed that the flow is governed by multiple frequencies under the conditions where the flow visualization results showed cellular structures in the wake. Additionally, the flow is governed by a single dominant frequency peak where spanwise perturbations are minimum and the flow exhibits a lock-on phenomenon.

(5) Both the oscillation amplitude and forcing frequency impact the lock-on parameter space. With increasing oscillation amplitude, the range of forcing frequencies for which the wake is locked onto the cylinder frequency expands.

(6) The value of  $C_D$  for a stationary tapered cylinder was  $\sim 10\%$ – $15\%$  less than a stationary straight cylinder for various Reynolds number confirming the observation of Gaster [3] and Bosch and Guterres [38].

(7) Maximum values of  $C_D$  are achieved when the forcing frequency enters the lock-on zone, which supports earlier numerical investigations on a straight circular rotationally oscillating cylinder [57,58].

(8) The maximum value of  $C_D$  increases as the oscillation amplitude is increased from  $\pi/2$  to  $3\pi/4$ . Additionally, when the forcing frequency leaves the lock-on region the reduction in drag coefficient is more for higher amplitude ( $\theta_0 = 3\pi/4$ ) as compared to lower amplitude ( $\theta_0 = \pi/2$ ).

(9) An increase in  $C_D$  is observed when a three-dimensional mode (mode Y) in the wake of an oscillating cylinder is observed.

#### ACKNOWLEDGMENTS

The authors wish to acknowledge the support provided by the Grant No. ARDB/01/1031875/M/I from the Aeronautics Research and Development Board (ARDB), DRDO (India).

- 
- [1] A. Roshko, On the development of turbulent wakes from vortex streets, National Advisory Committee for Aeronautics Technical Note 1191, California Institute of Technology, 1953.
  - [2] M. Gaster, Vortex shedding from slender cones at low Reynolds numbers, *J. Fluid Mech.* **38**, 565 (1969).
  - [3] M. Gaster, Vortex shedding from circular cylinders at low Reynolds numbers, *J. Fluid Mech.* **46**, 749 (1971).
  - [4] S. Taneda, Experimental investigation of vortex streets, *J. Phys. Soc. Jpn.* **20**, 1714 (1965).
  - [5] M. Hammache and M. Gharib, An experimental study of the parallel and oblique vortex shedding from circular cylinders, *J. Fluid Mech.* **232**, 567 (1991).
  - [6] C. Williamson, Oblique and parallel modes of vortex shedding in the wake of a circular cylinder at low Reynolds numbers, Technical Report, California Institute of Technology Pasadena Graduate Aeronautical Labs, 1989.
  - [7] D. Jespersen and C. Levit, Numerical simulation of flow past a tapered cylinder, in *29th Aerospace Sciences Meeting* (AIAA, California, 1991), p. 751.
  - [8] P. S. Piccirillo and C. Van Atta, An experimental study of vortex shedding behind linearly tapered cylinders at low Reynolds number, *J. Fluid Mech.* **246**, 163 (1993).
  - [9] S. Kumar and K. Poddar, An experimental study of near wake structure behind linearly tapered cylinders, *Aeronaut. Soc. India J.* **48**, 34 (1996).
  - [10] S. Kumar and K. Poddar, Control of near wake structure behind straight and linearly tapered cylinders, *Aeronaut. Soc. India J.* **52**, 147 (2000).
  - [11] B. Valles, H. Andersson, and C. Jenssen, Oblique vortex shedding behind tapered cylinders, *J. Fluids Struct.* **16**, 453 (2002).

- [12] P. Parnaudeau, D. Heitz, E. Lamballais, and J.-H. Silvestrini, Direct numerical simulations of vortex shedding behind cylinders with spanwise linear nonuniformity, *J. Turbul.* **8**, N13 (2007).
- [13] V. D. Narasimhamurthy, H. I. Andersson, and B. Pettersen, Steady viscous flow past a tapered cylinder, *Acta Mech.* **206**, 53 (2009).
- [14] J. Visscher, B. Pettersen, and H. I. Andersson, Experimental study on the wake behind tapered circular cylinders, *J. Fluids Struct.* **27**, 1228 (2011).
- [15] K. Bargi, V. Tamimi, and M. Zeinoddini, VIV of tapered cylinders: 3D LES numerical simulation, *Intl. J. Maritime Tech.* **3**, 17 (2015).
- [16] A. K. De and S. Sarkar, Three-dimensional wake dynamics behind a tapered cylinder with large taper ratio, *Phys. Fluids* **32**, 063604 (2020).
- [17] C. Williamson and A. Roshko, Vortex formation in the wake of an oscillating cylinder, *J. Fluids Struct.* **2**, 355 (1988).
- [18] A. Techet, F. Hover, and M. Triantafyllou, Vortical patterns behind a tapered cylinder oscillating transversely to a uniform flow, *J. Fluid Mech.* **363**, 79 (1998).
- [19] A. Radi, M. C. Thompson, A. Rao, K. Hourigan, and J. Sheridan, Experimental evidence of new three-dimensional modes in the wake of a rotating cylinder, *J. Fluid Mech.* **734**, 567 (2013).
- [20] A. Rao, J. Leontini, M. C. Thompson, and K. Hourigan, Three-dimensionality in the wake of a rotating cylinder in a uniform flow, *J. Fluid Mech.* **717**, 1 (2013).
- [21] A. Rao, J. S. Leontini, M. C. Thompson, and K. Hourigan, Three-dimensionality in the wake of a rapidly rotating cylinder in uniform flow, *J. Fluid Mech.* **730**, 379 (2013).
- [22] N. G. Chikkam and S. Kumar, Flow past a rotating hydrophobic/nonhydrophobic circular cylinder in a flowing soap film, *Phys. Rev. Fluids* **4**, 114802 (2019).
- [23] P. T. Tokumaru and P. E. Dimotakis, Rotary oscillation control of a cylinder wake, *J. Fluid Mech.* **224**, 77 (1991).
- [24] B. Thiria, S. Goujon-Durand, and J. Wesfreid, The wake of a cylinder performing rotary oscillations, *J. Fluid Mech.* **560**, 123 (2006).
- [25] S. Kumar, C. Lopez, O. Probst, G. Francisco, D. Askari, and Y. Yang, Flow past a rotationally oscillating cylinder, *J. Fluid Mech.* **735**, 307 (2013).
- [26] P. Sunil, S. Kumar, and K. Poddar, Flow past a rotationally oscillating cylinder with an attached flexible filament, *J. Fluid Mech.* **930**, A3 (2022).
- [27] R. Antonia and S. Rajagopalan, Determination of drag of a circular cylinder, *AIAA J.* **28**, 1833 (1990).
- [28] E. Konstantinidis and S. Balabani, Symmetric vortex shedding in the near wake of a circular cylinder due to streamwise perturbations, *J. Fluids Struct.* **23**, 1047 (2007).
- [29] Y. Zhou, M. M. Alam, H. Yang, H. Guo, and D. Wood, Fluid forces on a very low Reynolds number airfoil and their prediction, *Int. J. Heat Fluid Flow* **32**, 329 (2011).
- [30] S. Sharma and P. Deshpande, Kutta–Joukowski theorem in viscous and unsteady flow, *Exp. Fluids* **52**, 1581 (2012).
- [31] L.-H. Feng and J.-J. Wang, Synthetic jet control of separation in the flow over a circular cylinder, *Exp. Fluids* **53**, 467 (2012).
- [32] G. S. He, N. Li, and J. J. Wang, Drag reduction of square cylinders with cut-corners at the front edges, *Exp. Fluids* **55**, 1745 (2014).
- [33] J. Brennan, D. Fairhurst, R. Morris, G. McHale, and M. Newton, Investigation of the drag reducing effect of hydrophobized sand on cylinders, *J. Phys. D* **47**, 205302 (2014).
- [34] P. A. Dewey, B. M. Boschitsch, K. W. Moored, H. A. Stone, and A. J. Smits, Scaling laws for the thrust production of flexible pitching panels, *J. Fluid Mech.* **732**, 29 (2013).
- [35] J. H. Buchholz, R. P. Clark, and A. J. Smits, Thrust performance of unsteady propulsors using a novel measurement system, and corresponding wake patterns, *Exp. Fluids* **45**, 461 (2008).
- [36] C. v. Wieselsberger, Neuere Feststellungen über die Gesetze des Flüssigkeits und Luftwiderstands, *Phys. Z.* **22**, 321 (1921).
- [37] M. Zdravkovich, Conceptual overview of laminar and turbulent flows past smooth and rough circular cylinders, *J. Wind Eng. Ind. Aerodyn.* **33**, 53 (1990).

- [38] H. Bosch and R. Guterres, Wind tunnel experimental investigation on tapered cylinders for highway support structures, *J. Wind Eng. Ind. Aerodyn.* **89**, 1311 (2001).
- [39] C. Lin and S.-C. Hsieh, Convection velocity of vortex structures in the near wake of a circular cylinder, *J. Eng. Mech.* **129**, 1108 (2003).
- [40] A. Ahmed, On the wake of a circular cylinder with nodal and saddle attachment, *J. Fluids Struct.* **26**, 41 (2010).
- [41] H. Eisenlohr and H. Eckelmann, Vortex splitting and its consequences in the vortex street wake of cylinders at low Reynolds number, *Phys. Fluids* **1**, 189 (1989).
- [42] J. Gerrard, The mechanics of the formation region of vortices behind bluff bodies, *J. Fluid Mech.* **25**, 401 (1966).
- [43] B. Thiria and J. Wesfreid, Stability properties of forced wakes, *J. Fluid Mech.* **579**, 137 (2007).
- [44] P. Poncet, Vanishing of mode B in the wake behind a rotationally oscillating circular cylinder, *Phys. Fluids* **14**, 2021 (2002).
- [45] G. I. Taylor, Experiments on the motion of solid bodies in rotating fluids, *Proc. R. Soc. London* **104**, 213 (1923).
- [46] R. Hide and A. Ibbetson, An experimental study of “Taylor columns”, *Icarus* **5**, 279 (1966).
- [47] T. K. Sengupta and D. Patidar, Flow past a circular cylinder executing rotary oscillation: Dimensionality of the problem, *Phys. Fluids* **30**, 093602 (2018).
- [48] S. Bhattacharyya, I. H. Khan, S. Verma, S. Kumar, and K. Poddar, Experimental investigation of three-dimensional modes in the wake of a rotationally oscillating cylinder, *J. Fluid Mech.* **950**, A10 (2022).
- [49] E. Anderson and A. Szewczyk, Effects of a splitter plate on the near wake of a circular cylinder in 2- and 3-dimensional flow configurations, *Exp. Fluids* **23**, 161 (1997).
- [50] J. Wu, J. Sheridan, J. Soria, and M. Welsh, An experimental investigation of streamwise vortices in the wake of a bluff body, *J. Fluids Struct.* **8**, 621 (1994).
- [51] P. Poncet, R. Hildebrand, G.-H. Cottet, and P. Koumoutsakos, Spatially distributed control for optimal drag reduction of the flow past a circular cylinder, *J. Fluid Mech.* **599**, 111 (2008).
- [52] D. L. Jacono, J. S. Leontini, M. C. Thompson, and J. Sheridan, Modification of three-dimensional transition in the wake of a rotationally oscillating cylinder, *J. Fluid Mech.* **643**, 349 (2010).
- [53] J. H. Silvestrini and E. Lamballais, Direct numerical simulation of oblique vortex shedding from a cylinder in shear flow, *Int. J. Heat Fluid Flow* **25**, 461 (2004).
- [54] A. Okajima, H. Takata, and T. Asanuma, Viscous flow around a rotationally oscillating circular cylinder, ISAS report, Institute of Space and Aeronautical Science, University of Tokyo **40**, 311 (1975).
- [55] F. Mahfouz and H. Badr, Flow structure in the wake of a rotationally oscillating cylinder, *J. Fluids Eng.* **122**, 290 (2000).
- [56] J. Wu, J. Mo, and A. Vakili, On the wake of a cylinder with rotational oscillations, in *2nd Shear Flow Conference* (1989), p. 1024.
- [57] M. Cheng, Y. Chew, and S. Luo, Numerical investigation of a rotationally oscillating cylinder in mean flow, *J. Fluids Struct.* **15**, 981 (2001).
- [58] X.-Y. Lu and J. Sato, A numerical study of flow past a rotationally oscillating circular cylinder, *J. Fluids Struct.* **10**, 829 (1996).